

LA-UR-18-22657 (Accepted Manuscript)

An integrated boundary approach for colloidal suspensions simulated using smoothed dissipative particle dynamics

Petsev, Nikolai Dimitrov
Leal, L. Gary
Shell, M. Scott

Provided by the author(s) and the Los Alamos National Laboratory (2019-02-20).

To be published in: Computers & Fluids

DOI to publisher's version: 10.1016/j.compfluid.2018.11.025

Permalink to record: <http://permalink.lanl.gov/object/view?what=info:lanl-repo/lareport/LA-UR-18-22657>

Disclaimer:

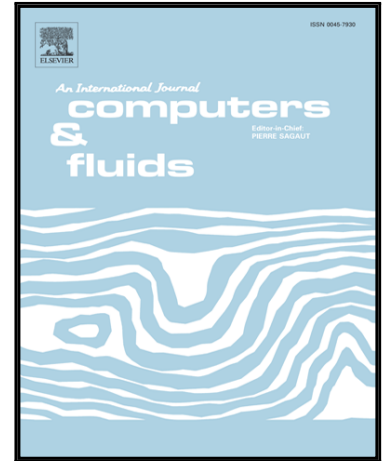
Approved for public release. Los Alamos National Laboratory, an affirmative action/equal opportunity employer, is operated by the Los Alamos National Security, LLC for the National Nuclear Security Administration of the U.S. Department of Energy under contract DE-AC52-06NA25396. Los Alamos National Laboratory strongly supports academic freedom and a researcher's right to publish; as an institution, however, the Laboratory does not endorse the viewpoint of a publication or guarantee its technical correctness.

Accepted Manuscript

An integrated boundary approach for colloidal suspensions simulated using smoothed dissipative particle dynamics

Nikolai D. Petsev , L. Gary Leal , M. Scott Shell

PII: S0045-7930(18)30906-X
DOI: <https://doi.org/10.1016/j.compfluid.2018.11.025>
Reference: CAF 4067



To appear in: *Computers and Fluids*

Received date: 10 May 2018
Revised date: 30 August 2018
Accepted date: 23 November 2018

Please cite this article as: Nikolai D. Petsev , L. Gary Leal , M. Scott Shell , An integrated boundary approach for colloidal suspensions simulated using smoothed dissipative particle dynamics, *Computers and Fluids* (2018), doi: <https://doi.org/10.1016/j.compfluid.2018.11.025>

This is a PDF file of an unedited manuscript that has been accepted for publication. As a service to our customers we are providing this early version of the manuscript. The manuscript will undergo copyediting, typesetting, and review of the resulting proof before it is published in its final form. Please note that during the production process errors may be discovered which could affect the content, and all legal disclaimers that apply to the journal pertain.

Highlights

- Integrated boundaries in particle-based simulations reduce computational cost
- Analytical integrated boundary expressions for spherical colloids are derived
- Integrated boundaries allow for modeling colloids at arbitrary Re and Pe numbers
- Tests with integrated boundaries in low-Re limit reproduce expected Stokes' drag
- Integrated strategy gives correct diffusive behavior for Brownian sphere

ACCEPTED MANUSCRIPT

An integrated boundary approach for colloidal suspensions simulated using smoothed dissipative particle dynamics

Nikolai D. Petsev,

Theoretical Division, Los Alamos National Laboratory, Los Alamos, New Mexico 87545, USA

L. Gary Leal, and M. Scott Shell

Department of Chemical Engineering, University of California at Santa Barbara, Santa Barbara, California 93106-5080, USA

Abstract

In particle-based continuum solvers such as smoothed particle hydrodynamics (SPH) and smoothed dissipative particle dynamics (SDPD), one of the most significant challenges is the treatment of solid boundaries like walls and colloidal particles, whose presence leads to a truncation of the integral approximation, and hence, error in the numerical solution. In this work, we describe an integrated boundary framework for modeling colloidal suspensions composed of rigid spherical particles. The integral corresponding to the colloid's contribution is analytically evaluated, giving a simple and computationally inexpensive approach relative to conventional boundary particle techniques. We formulate a thermodynamically-consistent version of this top-down method for mesoscale simulations, in which the fluid exchanges momentum with the

suspended particles due to thermal fluctuations, giving a framework for modeling the dynamics of colloids at arbitrary Reynolds and Péclet numbers. The resulting evolution equations are validated for a single colloidal particle in a fluid at constant temperature. This simple approach requires $\sim N_c (\rho/m) R_c^2$ fewer pair force calculations relative to traditional boundary particle strategies, where N_c is the number of colloids in the system, R_c is the colloid radius, ρ is the colloid mass density, and m is the mass of the SDPD particles. In addition, the use of integrated boundaries removes the need for rigid body constraint dynamics, giving an elegant and efficient basis for large-scale simulations of colloidal suspensions that is general and does not make any physical assumptions about the flow.

1. Introduction

Smoothed particle hydrodynamics (SPH) [1–4] is a particle-based continuum solver, originally formulated for the simulation of astrophysical phenomena and more recently adapted to problems in solid and fluid mechanics. In this numerical simulation scheme for hydrodynamic problems, a fluid is decomposed into a collection of volumes or so-called “particles” whose positions, velocities, and other properties evolve in time following appropriately discretized forms of the transport equations. This type of meshless, Lagrangian strategy to computational fluid dynamics offers a number of advantages for certain types of problems over traditional Eulerian grid-based methods, such as applications involving interfaces and deformable or free boundaries [3]. In addition, these techniques incorporate advection in a natural way and are easily extensible to include more complex physics (e.g. polymer melts and suspensions can be

treated by tethering fluid volumes with a harmonic potential). SPH has been applied to a diverse set of macroscopic fluid problems [5–11].

Importantly, SPH can also be reformulated using the GENERIC formalism [12–14] to account for entropy production and include scale-dependent thermal fluctuations in the relevant hydrodynamic variables (e.g. momentum, concentration, etc.) associated with each material volume [15]. This thermodynamically-consistent version of SPH is known as smoothed dissipative particle dynamics (SDPD), and features a random noise term in the equations of motion that introduces stochastic fluxes of momentum and solute between particles [15,16], giving a generalization of SPH from the macroscale to the mesoscale. SDPD has been used for a number of applications ranging from polymer physics [17,18] and pinned DNA dynamics under shear [19] to blood flow modeling [20]. SDPD has also been used to model colloidal particles dispersed in a fluid medium [17,21], a problem ubiquitous in physics and relevant to numerous industrial applications including paints, slurries, composite materials, and ceramics. These kinds of suspensions are generally composed of colloids that interact through interparticle (e.g. electrostatic, van der Waals, etc.), hydrodynamic, and thermal forces, a consequence of their dimensions ranging from nanometers to microns, and are thus ideally suited for modeling using SDPD.

One major challenge in adapting these particle-based approaches to problems in continuum mechanics, including the SDPD application to colloidal dispersions, is the presence of solid interfaces and rigid objects. When considering low Reynold's number flows in particular, it is often critical to impose the kinematic and no-slip boundary conditions precisely at the solid-liquid interface. An example is the collision between two particles, where it is known that the particle surfaces may pass exceedingly close together. To this end, numerous techniques for

applying boundary conditions in large-scale SPH problems have been proposed over the years. For example, boundaries may be introduced by renormalizing the integral approximation for points near surfaces [22–24,23], modifying the smoothing kernel [25–27], or through Taylor series expansions [24]. Most often, they are modeled through “ghost” boundary particles frozen on a lattice inside the solid, or ghost particles generated on-the-fly at every time-step [4,8]. These ghost particles exert repulsive forces on the fluid particles in order to enforce the kinematic boundary condition and prevent boundary penetration, as well as additional interactions that impose other constraints on the flow near the surface. For instance, Morris et al. freeze particles in place for solid objects and assign fictitious, “virtual” velocities to them by extrapolating the velocity profile into the surface such that the modified viscous force gives no-slip along a well-defined spatial interface [6]. These types of algorithms for extending functions into the boundary domain successfully modify the particle dynamics to impose the no-slip condition [28], though they require costly additional pair force calculations.

An elegant solution was partly provided by Takeda et al. [29], who integrated out the contribution of the “ghost” boundary particles for the planar boundary surface case and removed the need for computing these additional forces. A similar approach has been used in simulations using the so-called “dissipative particle dynamics” (DPD) method [30,31], where solid objects interact with fluid particles through an effective force contribution that replaces individual boundary particle interactions [32–34]. Integrated boundary forces also appear in hybrid molecular-continuum simulations in order to minimize disturbances and apply the correct pressure to zones with MD atoms located near the MD-continuum interface [35]. For the first time, we apply this perspective to suspensions modeled through SDPD and obtain simple boundary expressions that allow for more efficient simulations of many-body colloidal

dispersions. In addition to avoiding the use of iterative schemes for enforcing rigid bonds between the particles comprising the solid body, this strategy reduces the number of force calculations by $\sim N_c (\rho/m) R_c^2 \kappa h$, within a constant pre-factor, where N_c is the number of colloids in the system, R_c is the colloidal particle radius, and m and ρ are the SDPD particles mass and fluid/particle mass density, respectively. This scaling behavior assumes the main reduction in pair interactions is given by removing interactions between fluid-solid SDPD particles involving fluid particles in a thin shell surrounding the colloid with width determined by the interaction distance κh . The number of fluid particles within this shell is, to the leading order, $4\pi(\rho/m) R_c^2 \kappa h$. Each one of these fluid particles is close enough to the colloid to interact with at least one solid SDPD particle inside it. This analysis also treats the colloid as a hollow sphere, with solid SDPD particles far from the surface removed from the computation for efficiency. In this case, the scaling behavior described above dominates over the reduction in rigid-body solid-solid pair interactions in the solid particle. Clearly for simulations involving a large number of colloids N_c , or simulations having colloidal particles that are made up of a large number of boundary subparticles, $R_c \gg \kappa h$, this reduction becomes significant and results in major computational savings. However, for very dilute suspensions, the large amounts of fluid particles in the bulk will determine the scaling behavior and savings using the integrated boundary scheme are modest.

One popular alternative to SDPD for nano- and micro-scale suspensions is dissipative particle dynamics (DPD) [36–38], a bottom-up approach where the fluid is divided into clumps of molecules that interact through coarse-grained, softly-repulsive interactions in addition to dissipative and fluctuating ones. However, the free parameters in the DPD model are related to fluid properties like viscosity in an indirect fashion (i.e., kinetic theory or a simulation is required

to compute them), and there is no physical length scale associated with the DPD interactions [15,17]. SDPD addresses these issues, and hence the integrated SDPD approach considered in this work can be viewed as a top-down alternative to similar integrated strategies in DPD that is rigorously obtained from the continuum transport equations. Colloidal dispersions may also be modeled using Brownian dynamics, where the solvent is treated implicitly and the velocity of each suspended particle is evolved according to the Langevin equation. Brownian dynamics offers a computationally inexpensive basis for large-scale modeling of dilute suspensions, though it typically ignores hydrodynamic interactions between colloids and is only valid in the zero Péclet number limit (though hydrodynamic interactions may be incorporated through the Oseen tensor for the friction terms [39]). It may also be generalized to the so-called “Stokesian dynamics” method [40–43], which includes hydrodynamic interactions between particles and is applicable to any Péclet number, though it assumes creeping flow and therefore ignores inertia altogether. Inertial terms are included when using a Lattice-Boltzmann description for the fluid [44,45], though this approach is quantitative and traditionally applicable when density variations are small, i.e. for systems with incompressible fluids.

Unlike these approaches, the SDPD work presented here is a fluctuating Lagrangian equivalent to “direct numerical simulation”, which involves no physical approximation for the flow beyond the usual continuum assumption [46], and is valid for arbitrary Reynolds and Péclet numbers, including scenarios where inertia is important. While we only consider incompressible fluids in this work, the approach presented here is extensible to compressible cases. Moreover, this approach may be applicable to a limited range of non-spherical geometries (e.g. spheroids). Hence, we provide a framework for treating colloidal particles as continuum solid objects in SDPD, rather than being composed of discrete particles that necessitate the calculation of costly

additional pair interactions and rigid-body dynamics. This gives an approach that is less computationally expensive and more elegant than traditional boundary particle methods, since every fluid particle that is near a boundary receives a single contribution to its evolution equation due to the nearby colloid. In particular, we obtain analytical expressions for simple planar and spherical boundaries, and incorporate scale-dependent thermal fluctuations for stochastic fluxes of momentum between the fluid and boundary. In Section 2, we provide a brief summary of SDPD and the problem of boundaries. Section 3 introduces the integrated boundary approach and gives analytical results for approximating functions near surfaces with planar and spherical geometries. Sections 4-7 describe simple validation tests in the incompressible creeping flow limit since those results can be compared to known analytical solutions.

Note that Newtonian volumes of fluid exchange momentum due to three distinct types of forces: *(i)* pressure forces, *(ii)* viscous interactions, and *(iii)* random fluctuations. Each one of these contributions is considered separately in the following sections. In Section 4, we focus on the first contribution to the particles' equations of motion *(i)* and develop an integrated pressure force that prevents fluid particles from penetrating the solid boundary. A boundary term for the Laplacian operator, which is essential to a number of transport problems, is derived in Section 5. The resulting boundary term gives the viscous interaction *(ii)*. These viscous forces also give a net torque that acts on the colloid, and we derive an expression for the total torque due to surrounding fluid particles in Section 6. We then consider the random force between particles *(iii)* and generalize the boundary approach to the mesoscale by allowing the fluid to stochastically exchange linear and angular momenta with the fluid particles in Section 7. Finally, in Section 8 we perform full-scale simulations of a single colloidal sphere using these results and

show that they reproduce the correct diffusive behavior, indicating that our equations give the correct fluctuation-dissipation balance.

2. Smoothed Dissipative Particle Dynamics

To illustrate the problem posed by solid boundaries when using smoothed particle methods, we begin with a brief overview of this subject. A more comprehensive review can be found in Refs. [3,4]. The key to these approaches is the so-called “integral approximation”, where a function $f(\mathbf{r})$ (assumed continuous on Ω) at some point \mathbf{r} is written as,

$$\langle f \rangle(\mathbf{r}) = \frac{1}{\gamma(\mathbf{r})} \int_{\Omega} f(\mathbf{r}') W(\mathbf{r} - \mathbf{r}', h) d\mathbf{r}'. \quad (1)$$

In the above expression, we have the Shepard normalization factor, which is typically unity due to the normalization requirement for the smoothing function,

$$\gamma(\mathbf{r}) = \int_{\Omega} W(\mathbf{r} - \mathbf{r}', h) d\mathbf{r}'. \quad (2)$$

In this work, the bracket $\langle \rangle$ indicates the integral approximation. The smoothing kernel W is a normalized, positive function with compact support determined by the “smoothing length” h , which reduces to the Dirac delta function in the limit $h \rightarrow 0$. Later, we decompose the fluid domain into a collection of fluid “particles” and write these integrals as sums over the neighboring particles. Note that the delta function requirement for W implies that Eq.(1) becomes exact in the limit $h \rightarrow 0$. Hence, h controls the accuracy of the numerical solution in SPH; choosing a smaller value gives a more precise result, but requires using more particles to give an

improved approximation of Eq.(1), and hence more calculated pair interactions over the full fluid domain. The error associated with the approximation $\langle f \rangle(\mathbf{r})$ scales as $O(h^2)$.

In order to obtain the SPH approximation to a function, the problem domain is discretized into a collection of N fluid volumes or “particles”, in which case the integral in Eq.(1) is approximated as the sum

$$\langle f \rangle(\mathbf{r}) \approx \sum_j^N \frac{m_j}{\rho_j} f(\mathbf{r}_j) W(\mathbf{r} - \mathbf{r}_j, h). \quad (3)$$

Here, m_j and ρ_j are the mass and density of the j th particle, respectively, and we assume that the domain is not truncated by a boundary and the Shepard factor therefore is $\gamma=1$. The sum extends over all the particles in the system, but the compact support condition for the function W ensures that only nearby ones contribute to the average, and the sum is actually performed over all the particles within a sphere with radius κh (where κ is a constant that controls this cut-off radius for interaction). Similar sum-over-particles approximations can be obtained for spatial derivatives of functions as well. The application of the integral and particle approximations to the hydrodynamic equations is the basis for SPH, giving equations of motion for the particles that are used to evolve their properties such as positions, velocities, and densities using integrators typically used in molecular dynamics (MD) simulations. For example, the incompressible Navier-Stokes equation in the Lagrangian frame is given by [47]

$$\rho \frac{d\mathbf{v}}{dt} = -\nabla p + \eta \nabla^2 \mathbf{v}. \quad (4)$$

In this expression, the differential on the left-hand-side is a material derivative, ρ is the fluid mass density, and η is the viscosity. Applying the integral and particle approximation to the right-hand-side (i.e. the forces acting on a fluid element) gives the following evolution equation

for the momentum of the i th fluid particle, with pairwise interactions between fluid particles resulting from the symmetrized discretization [6],

$$m_i \frac{d\mathbf{v}_i}{dt} = - \sum_{j=1}^N m_i m_j \left(\frac{p_i}{\rho_i^2} + \frac{p_j}{\rho_j^2} \right) \frac{\partial W_{ij}}{\partial r_{ij}} \mathbf{e}_{ij} + 2\eta \sum_{j=1}^N \frac{m_i m_j}{\rho_i \rho_j} \left(\frac{1}{|\mathbf{r}_{ij}|} \frac{\partial W_{ij}}{\partial r_{ij}} \right) \mathbf{v}_{ij}. \quad (5)$$

Here, m_i , p_i , and ρ_i give the mass, pressure, and density of the i th particle, respectively. \mathbf{v}_{ij} is the relative velocity between particles i and j , $\mathbf{v}_{ij} \equiv \mathbf{v}_i - \mathbf{v}_j$, and $\mathbf{e}_{ij} \equiv \mathbf{r}_{ij} / |\mathbf{r}_{ij}|$ with $\mathbf{r}_{ij} \equiv \mathbf{r}_i - \mathbf{r}_j$.

In order to obtain the thermodynamically-consistent version of SPH known as SDPD, we include thermal fluctuations in the velocity field for simulations at mesoscopic length scales. For the isothermal incompressible case, an additional term for the stochastic contribution to momentum $m_i d\tilde{\mathbf{v}}_i$ is included in the equation of motion given by Eq.(5) with the form [15,21,48]

$$m_i d\tilde{\mathbf{v}}_i = \sum_{j=1}^N A_{ij} d\hat{\mathbf{W}}_{ij} \cdot \mathbf{e}_{ij}. \quad (6)$$

$d\mathbf{W}_{ij}$ is a tensor of Brownian process increments and $d\hat{\mathbf{W}}_{ij}$ is the traceless, symmetric part of $d\mathbf{W}_{ij}$. Note that the smoothing function W_{ij} and tensor of Gaussian increments $d\mathbf{W}_{ij}$ are distinct quantities, and we use this nomenclature for historical reasons. The noise coefficient A_{ij} is determined through the fluctuation-dissipation theorem, giving [15,21,48]

$$A_{ij} = \left[- \frac{8\eta m_i m_j k_B T}{\rho_i \rho_j} \left(\frac{1}{|\mathbf{r}_{ij}|} \frac{\partial W_{ij}}{\partial r_{ij}} \right) \right]^{1/2}. \quad (7)$$

When fluctuations appear in the equations of motion, the parameter h takes on a slightly different meaning. Previously, h controlled the precision of the numerical solution, similar to the level of mesh refinement in a finite-element calculation. In SDPD, however, h controls the size of each particle, which is interpreted as a fluid volume locally in equilibrium. Decreasing the size of a

thermodynamic system produces greater relative thermal fluctuations. Hence, a smaller h gives finer particles subject to larger fluctuations, whereas increasing h results in more massive SDPD particles with diminished fluctuations. In other words, when thermal noise is included, adjusting h actually produces distinct particle dynamics by changing the coarse-graining level, and thus the relevance of thermodynamic fluctuations [17].

The problem posed by boundaries is immediately apparent when considering the integrals in Eqs.(1) and (2), which are truncated by the interface for any point \mathbf{r} located near a boundary. From the particle perspective [Eq.(3)], this truncation corresponds to a particle deficiency when summing over neighbors in the support domain of points near the surface. In order to deal with this issue, boundary or “ghost” particles are typically introduced to represent the solid surface. When using ghost particles in SPH, it is necessary to assign modified velocities to these particles and take additional measures in order to enforce a boundary condition at an arbitrarily-specified surface. Takeda et al. linearly extrapolate the function into the boundary in order to enforce no-slip precisely at the fluid-solid interface [29], though they only consider planar boundaries. Similarly, Morris et al. assign fictitious values of the function to boundary ghost particles such that for any pair interaction, the correct boundary condition is met [6]. This is achieved by using the value of the function in the fluid [$f(\mathbf{r})$], the value of the function in the wall [$f(\mathbf{r}')$], and the distances of the fluid and wall points relative to the boundary (Δz and $\Delta z'$, respectively) to determine a modified function difference $f(\mathbf{r}) - f(\mathbf{r}')$. In other words, it is possible to perform a linear extrapolation to determine what value must be assigned to the wall point, $f(\mathbf{r}')$ in order to enforce the boundary condition $f(\mathbf{r} = S) = f_w$, where S denotes the boundary and f_w is a constant. This gives the relationship [6]

$$f(\mathbf{r}) - f(\mathbf{r}') = \left(1 + \frac{\Delta z'}{\Delta z}\right) [f(\mathbf{r}) - f_w]. \quad (8)$$

As an example, when calculating the relative velocity between a fluid particle and a ghost particle in Eq.(5), Eq.(8) suggests that it can be replaced by the velocity of the fluid particle relative to the wall, where this velocity difference is rescaled by a factor that depends on the distances of the fluid and ghost particles from the boundary, $\beta = 1 + \Delta z' / \Delta z$ (see Figs. 1 and 3). This ensures that the fluid velocity assumes the wall value precisely at the liquid-solid interface when the full velocity field is computed, though it requires including additional boundary particles and hence calculating a large number of additional pairwise interactions.

In this work, the particle deficiency issue near surfaces is remedied by assuming that functions are defined over a space extending into the boundary such that a Dirichlet boundary condition is imposed precisely at the interface between the solid and liquid. Then, the integral over the boundary part of the domain is evaluated analytically, giving a single contribution to the equations of motion for the boundary rather than requiring many additional pair force calculations. This is consistent with existing particle-based boundary approaches, where sums over particles for points near a boundary include both fluid and “ghost” wall particles. Therefore, the support domain for any point Ω does not only include the fluid domain, but consists of both the fluid and wall, i.e. $\Omega = \Omega_f + \Omega_w$ resulting in an additional integral over Ω_w that provides the necessary support for points near the boundary. Since the maximum interaction length between particles is given by κh , Ω_w is the set of points inside the boundary located within a distance κh from the liquid-solid interface (though as a convenient approximation, Ω_w may be defined as all points inside a surface or colloidal particle, including ones beyond this maximum interaction distance since they contribute weakly to the final expressions). The integral over Ω_w

ensures that the approximation in Eq.(1) is not truncated, and therefore in everything that follows we set the normalization factor γ [Eq.(2)] to unity.

The purpose of this paper is therefore to provide analytical results for the wall contribution resulting from integration over the wall domain Ω_w , when simulating colloidal suspensions. In particular, we have to compute three separate boundary results since the SDPD equations of motion Eqs.(5) and (6) feature three distinct terms, (i) a pressure force between particle pairs, (ii) a viscous interaction proportional to the particles' velocity difference, and (iii) a random force due to thermal stresses. In the following sections, we outline this general approach and derive integrated boundary terms corresponding to each of these contributions.

3. Approximation of Function near Boundary

In order to demonstrate how the integrated boundary approach works, we first discuss the simplest application: approximating a function near planar and spherical surfaces. Consider a point \mathbf{r} in a continuum fluid near a boundary. Using the integral approximation [Eq.(1)] and the linearity of the integral operator, we can write

$$\langle f \rangle(\mathbf{r}) = \int_{\Omega_f} f(\mathbf{r}') W(\mathbf{r} - \mathbf{r}', h) d\mathbf{r}' + \int_{\Omega_w} f(\mathbf{r}') W(\mathbf{r} - \mathbf{r}', h) d\mathbf{r}', \quad (9)$$

where Ω_f is the part of the support domain of \mathbf{r} that lies in the fluid, and Ω_w is the part inside the wall. Hence, we assume the function is defined and continuous over a space that extends into the boundary, $\Omega = \Omega_f + \Omega_w$. The first term in Eq.(9) is the familiar integral representation of a function and therefore does not merit further discussion; discretizing this part using the particle approximation yields the familiar SPH sum over nearby fluid particles for approximating a

function, Eq.(3). However, this sum is incomplete due to a deficiency of neighboring particles, a consequence of the neighboring boundary that occupies the space Ω_w . Hence, we are interested in the second integral in Eq.(9), which is due to the surface and compensates for this lack of surrounding particles,

$$f_w \int_{\Omega_w} W(\mathbf{r} - \mathbf{r}', h) d\mathbf{r}'. \quad (10)$$

In writing Eq.(10), Dirichlet boundary conditions are assumed, i.e. $f(\mathbf{r})$ adopts some constant value f_w at the boundary and can be pulled in front of the integral operator. In this section, we focus on Eq.(10), which is the contribution of the wall to the function's value at some point \mathbf{r} in the integral approximation. In principle, this quantity can be numerically determined for objects with complicated shapes and boundaries featuring local curvature, though in practice computing this integral may be challenging. Furthermore, the length scale characterizing surface features or curvature should be larger than length scale associated with each fluid particle, given by κh , similar to how the length scale for individual elements in a finite-element calculation should be much smaller than the radius of curvature of a boundary in order to accurately resolve the surrounding flow. A discussion of the errors associated with the integrated approach we describe below is provided in Sections 4-6.

3.1. Fluid Particle near Planar Boundary

Eq.(10) is analytically determined for a simple planar geometry assuming the kernel $W(|\mathbf{r} - \mathbf{r}'|, h)$ is Gaussian. Throughout this paper, we use the Gaussian kernel since it allows for straightforward integration of boundary terms to give elegant analytical expressions. The

accuracy and use of Gaussian smoothing functions is discussed in Ref. [49]. It is important to note that one of the requirements for smoothing kernels in SPH is compact support and therefore, in practice, when using a Gaussian smoothing function, the kernel is truncated beyond some point to satisfy this condition. Hence, we must integrate over a region that corresponds to a sphere surrounding the point \mathbf{r} where we are approximating the function, with size determined by the support domain of the point, namely κh . For a function evaluated at a point \mathbf{r} located a distance Δz from a flat surface with vector normal in the z -direction, we can therefore explicitly write the integral Eq.(10) using spherical coordinates,

$$f_w \int_{\Omega_w} W(\mathbf{r}-\mathbf{r}', h) d\mathbf{r}' \approx f_w \int_{\Delta z}^{\kappa h} dr \int_0^{2\pi} d\phi \int_0^{\theta_0} d\theta W(r, h) r^2 \sin \theta, \quad (11)$$

where we have defined $\theta_0 = \cos^{-1}(\Delta z / r)$ and the coordinate origin is set at the position \mathbf{r} in the fluid where $f(\mathbf{r})$ is approximated. Fig. 1 illustrates the variables used to write Eq.(11).

It is possible to arrive at the result in Eq.(11) from a different perspective. Assuming virtual or “ghost” particles are used for the boundary, the particle approximation to a function, Eq.(3), can be decomposed into a sum over fluid particles, and a sum over the wall particles within the point’s support domain,

$$\langle f \rangle(\mathbf{r}) \approx \sum_{j, \text{fluid}}^{N_f} \frac{m_j}{\rho_j} f(\mathbf{r}_j) W(\mathbf{r} - \mathbf{r}_j, h) + \sum_{j, \text{wall}}^{N_w} \frac{m_j}{\rho_j} f(\mathbf{r}_j) W(\mathbf{r} - \mathbf{r}_j, h). \quad (12)$$

We consider the second sum on the right hand side, which accounts for the wall particles' contribution to the sum,

$$\frac{m_w}{\rho_w} f_w \sum_{j, \text{wall}}^{N_w} W(\mathbf{r} - \mathbf{r}_j, h). \quad (13)$$

Here, we have again assumed Dirichlet boundary conditions [$f(\mathbf{r}) = f_w$ at the wall], as well as uniform masses m_w and densities ρ_w for the wall particles. This sum extends over the N_w wall particles that lie within a sphere with radius κh centered at \mathbf{r} . Similar to the derivation of the Lennard-Jones 9-3 potential, this sum-over-particles is replaced with an integral scaled by the particle number density of the wall $\nu_w = \rho_w / m_w$,

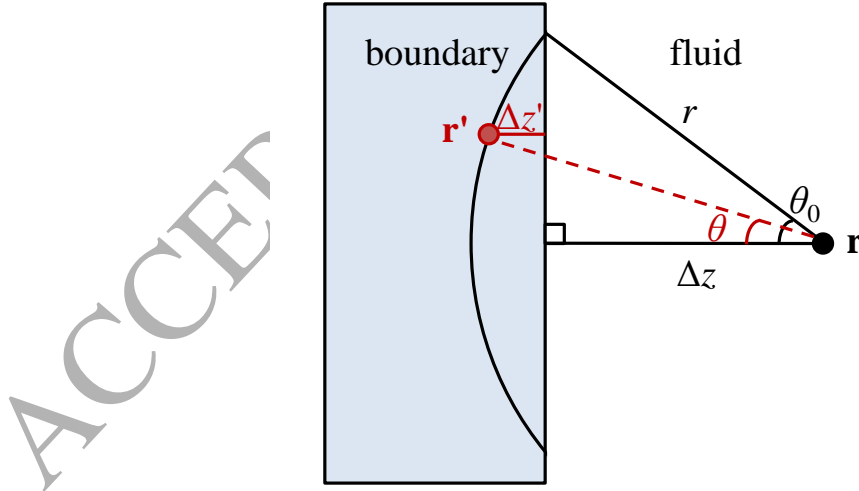


Fig. 1. Illustration showing the integration variables for the planar boundary contribution in spherical coordinates. The coordinate origin is set at the position in the fluid \mathbf{r} .

$$\frac{m_w}{\rho_w} f_w \sum_{j,wall}^{N_w} W(\mathbf{r} - \mathbf{r}_j, h) \approx \frac{m_w}{\rho_w} f_w v_w \int_{\Delta z}^{\kappa h} dr \int_0^{2\pi} d\phi \int_0^{\theta_0} d\theta W(r, h) r^2 \sin \theta. \quad (14)$$

Simplifying, we arrive at the same result as Eq.(11). This illustrates that, when deriving the integrated contributions of boundaries, we can begin either with the general integral approximation to a function, or from a fluid particle near a boundary composed of subparticles, and in both cases obtain the same result (Fig. 2).

Integrating Eq.(11) over the angular coordinates, we are left with

$$2\pi f_w \int_{\Delta z}^{\kappa h} dr W(r, h) r(r - \Delta z). \quad (15)$$

This expression is evaluated straightforwardly for the Gaussian smoothing function,

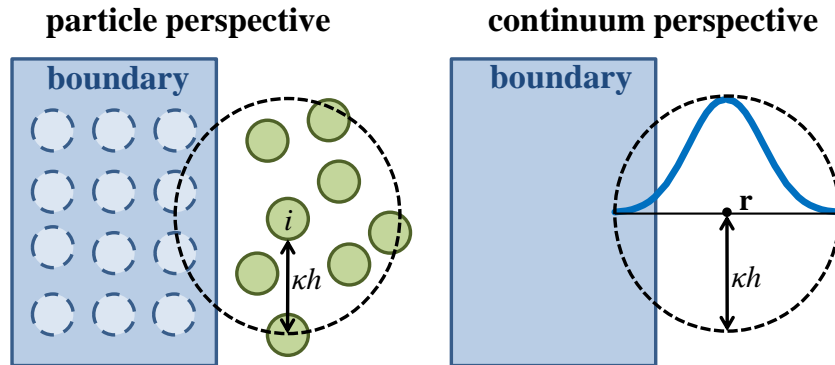


Fig. 2. Illustration of the particle perspective to the integrated boundary approach versus the continuum one. In the former, a function evaluated at the location of particle i depends on a sum over neighboring fluid particles (green) and virtual particles that comprise the boundary (light blue). The sum is partitioned into a sum over fluid particles, and one over wall particles that is rewritten as an integral. In the continuum perspective, the function evaluated at point r is obtained from an integral over a volume that is decomposed into an integral over the fluid domain, and an integral over the boundary, where the latter is evaluated explicitly.

$$W(r, h) = \frac{1}{\pi^{3/2} h^3} \exp\left[-\left(\frac{r}{h}\right)^2\right]. \quad (16)$$

Substituting Eq.(16) into Eq.(15) and applying the integral operator, we find that the exact contribution to the function near a boundary is

$$\frac{f_w}{2} \left[\operatorname{erf}(\kappa) - \operatorname{erf}\left(\frac{\Delta z}{h}\right) \right] - \frac{f_w}{\pi^{1/2} h} \exp(-\kappa^2) (\kappa h - \Delta z). \quad (17)$$

Note that the limit $\kappa \rightarrow \infty$, this reduces to the approximate expression derived by Takeda et al. for approximating the density near a boundary [29],

$$\frac{f_w}{2} \left[1 - \operatorname{erf}\left(\frac{\Delta z}{h}\right) \right]. \quad (18)$$

Eq.(18) is an approximation to the actual integral representation of a function equivalent to integrating over the entire boundary. In the limit $\kappa \rightarrow \infty$, we integrate to infinity and hence have additional contributions that would not exist with a properly local smoothing function. Due to the exponential kernel, however, these contributions are typically negligible. Throughout this work, we integrate over a finite domain whenever possible and provide the simpler $\kappa \rightarrow \infty$ expression afterwards. The limiting expression alone is provided when the more general case over a finite domain is not possible.

Therefore, the full approximation of a function at a point \mathbf{r} located near a boundary is

$$\begin{aligned} \langle f \rangle(\mathbf{r}) &= \sum_{j, \text{fluid}}^{N_f} \frac{m_j}{\rho_j} f(\mathbf{r}_j) W(\mathbf{r} - \mathbf{r}_j, h) \\ &+ \frac{f_w}{2} \left[\operatorname{erf}(\kappa) - \operatorname{erf}\left(\frac{\Delta z}{h}\right) \right] - \frac{f_w}{\pi^{1/2} h} \exp(-\kappa^2) (\kappa h - \Delta z), \end{aligned} \quad (19)$$

where Δz is the distance of the point \mathbf{r} from the surface. The summation is only over nearby fluid particles, and the second term on the right-hand-side gives the contribution of the boundary.

Without this term, Eq.(19) is simply the normal SPH approximation of a function. This additional contribution is included when the interface is located within the support domain of the point \mathbf{r} , $\Delta z \leq \kappa h$, and compensates for the lack of surrounding particles.

Eq.(19) can be applied to the density evaluated at each particle's position, a quantity that appears in the equations of motion in SPH [see Eq.(5)], giving

$$\begin{aligned} \langle \rho \rangle(\mathbf{r}_i) = & \sum_{j, \text{fluid}}^{N_f} m_j W(\mathbf{r}_i - \mathbf{r}_j, h) \\ & + \frac{\rho_w}{2} \left[\operatorname{erf}(\kappa) - \operatorname{erf}\left(\frac{\Delta z_i}{h}\right) \right] - \frac{\rho_w}{\pi^{1/2} h} \exp(-\kappa^2)(\kappa h - \Delta z_i). \end{aligned} \quad (20)$$

Here, Δz_i is the distance of the i th particle from the boundary. The sum in Eq.(20) is performed at each time-step to evolve the density of each particle. This is the so-called ‘‘summation density’’ approach, which now features an additional term due to the presence of a nearby solid object. The density update equation given by Eq.(20) matches the one used by Takeda et al. in the limit $\kappa \rightarrow \infty$. Note that assuming a constant density for the boundary does not reproduce peak pressures as accurately as evolving the densities of the wall particles [6], though we find it sufficient in the test studies that follow below.

3.2. Fluid Particle near Spherical Body

To apply this approach to suspensions composed of hard spheres, we evaluate Eq.(10) for a point in the fluid located near a solid spherical object. Note that the resulting expression is most accurate when the radius of the sphere is significantly larger than the smoothing length. Similar to Ref. [50], we write this integral in spherical coordinates by setting the coordinate origin at the point in the fluid \mathbf{r} ,

from the center of a solid spherical object having radius R_c and uniform density ρ_w is therefore given by

$$\begin{aligned} \langle \rho \rangle(\mathbf{r}_i) = & \sum_{j, \text{fluid}}^{N_f} m_j W(\mathbf{r}_i - \mathbf{r}_j, h) \\ & + \frac{\rho_w}{2} \left\{ \frac{h}{\pi^{1/2} R} \left[\exp(-A_+^2) - \exp(-A_-^2) \right] + G_- \right\}, \end{aligned} \quad (24)$$

where ρ_w is the mass density of the wall. For the tests provided in this work, we assume the mass density of the solid is the same as the fluid, and hence later when these strategies are applied to colloids, we consider neutrally buoyant particles.

4. Integrated Boundary Approximation for Pressure Term

We now consider the first of the three distinct forces that appear in the SDPD equation of motion, the conservative term due to the pressure distribution. Without the presence of boundary ghost particles to exert a pressure force, fluid particles may penetrate the solid interface. This is especially true for simulations of incompressible fluids, where the equation of state leads to strong repulsions between particle pairs that can drive them outside of the simulation box without a restraining force. Hence, an integrated pressure force prevents boundary penetration and enforces the kinematic boundary condition.

4.1. Pressure Force near Planar Boundary

Obtaining a symmetrized integrated expression for the pressure gradient boundary term is more intuitive and simple starting from the particle perspective, which is how we proceed in this section. The pressure force in SPH is the first term on the right-hand-side of Eq.(5). Splitting this summation into wall and fluid contributions, we again focus on the sum over the wall particles and assume a constant value for the density at the wall,

$$m_i \frac{d\mathbf{v}_i}{dt} = m_i m_w \left(\frac{p_i}{\rho_i^2} + \frac{p_w}{\rho_w^2} \right) \sum_{j, \text{wall}}^{N_w} \mathbf{r}_{ij} F_{ij}, \quad (25)$$

where

$$\nabla_i W_{ij} = -\mathbf{r}_{ij} F_{ij} \quad (26)$$

and $F_{ij} \equiv F(r_{ij}) \geq 0$. Here, we have p_w , which is the pressure of the wall particle. Following the approach of Bian et al. [21], we use a Neumann boundary condition for the solid-fluid particle pair interactions, $p_w = p_i$.

With the choice of Eq.(16) for the smoothing function, we have

$$F(r) = \frac{2}{\pi^{3/2} h^5} \exp \left[-\left(\frac{r}{h} \right)^2 \right]. \quad (27)$$

Note that components of the force in Eq.(25) parallel to the boundary will cancel due to symmetry. Hence, we only sum the component of this force that is perpendicular to the wall and apply the pressure boundary condition $p_w = p_i$,

$$m_i \frac{d\mathbf{v}_i}{dt} \Big|_{\mathbf{n}} = m_i m_w p_i \left(\frac{1}{\rho_i^2} + \frac{1}{\rho_w^2} \right) \sum_{j, \text{wall}}^N (\mathbf{r}_{ij} \cdot \mathbf{n}) \mathbf{n} F_{ij}. \quad (28)$$

Here, \mathbf{n} is the vector normal to the boundary. For a planar surface with normal in the z -direction, we replace the sum with the following integral,

$$-v_w m_i m_w p_i \left(\frac{1}{\rho_i^2} + \frac{1}{\rho_w^2} \right) \mathbf{n} \int_{-\infty}^{\infty} dX \int_{-\infty}^{\infty} dY \int_{-\infty}^{-\Delta z} dZZF \left[(X^2 + Y^2 + Z^2)^{1/2} \right]. \quad (29)$$

For simplicity, we allow the integral limits to extend to infinity, i.e. we make the approximation $\kappa \rightarrow \infty$. Substituting Eq.(27) into Eq.(29) and integrating gives the final result,

$$= \frac{\rho_w m_i p_i}{\pi^{1/2} h} \left(\frac{1}{\rho_i^2} + \frac{1}{\rho_w^2} \right) \exp \left[- \left(\frac{\Delta z}{h} \right)^2 \right] \mathbf{n}. \quad (30)$$

Hence, for a particle located within a distance κh of the wall, the equation of motion due to the pressure distribution features an additional contribution,

$$m_i \frac{d\mathbf{v}_i}{dt} \Big|_{press} = \sum_{j, fluid}^{N_f} m_i m_j \left(\frac{p_i}{\rho_i^2} + \frac{p_j}{\rho_j^2} \right) \mathbf{r}_{ij} F_{ij} + \frac{\rho_w m_i p_i}{\pi^{1/2} h} \left(\frac{1}{\rho_i^2} + \frac{1}{\rho_w^2} \right) \exp \left[- \left(\frac{\Delta z_i}{h} \right)^2 \right] \mathbf{n}. \quad (31)$$

Eq.(31) is readily extended to situations where the fluid particle is near a planar boundary with a vector normal in a different direction, or near multiple planar boundaries. In the general case, the particle has a separate boundary term in its equation of motion for each planar surface, where \mathbf{n} is the normal for each surface, and Δz_i is the corresponding separation distance. For the case of a particle near a corner where two surfaces meet, however, including a separate boundary term for each surface may not give accurate results since some boundary-fluid interactions will be double-counted where the boundaries intersect, and the integral of the kernel needs to be evaluated with additional care.

4.2. Pressure Force near Spherical Object

Near a spherical object, the integral due to the boundary is instead

$$\begin{aligned}
& m_i m_w \left(\frac{p_i}{\rho_i^2} + \frac{p_w}{\rho_w^2} \right) \sum_{j, \text{wall}}^{N_w} (\mathbf{r}_{ij} \cdot \mathbf{n}) \mathbf{n} F_{ij} \\
& = v_w m_i m_w \left(\frac{p_i}{\rho_i^2} + \frac{p_w}{\rho_w^2} \right) \mathbf{n} \int_{R-R_c}^{R+R_c} dr \int_0^{2\pi} d\phi \int_0^{\theta_0} d\theta r^3 \sin \theta \cos \theta F(r).
\end{aligned} \tag{32}$$

In this case, \mathbf{n} is defined as the vector normal to the sphere pointing in the direction of the fluid particle. Once again applying the condition $p_w = p_i$ and integrating over θ and ϕ ,

$$= \pi v_w m_i m_w p_i \left(\frac{1}{\rho_i^2} + \frac{1}{\rho_w^2} \right) \mathbf{n} \int_{R-R_c}^{R+R_c} dr r^3 F(r) \sin^2 \theta_0. \tag{33}$$

Substituting $F(r)$ and θ_0 , again specified through $R_c^2 = R^2 + r^2 - 2rR \cos \theta_0$, and integrating gives the final result,

$$= \frac{\rho_w m_i h p_i}{2R^2 \pi^{1/2}} \left(\frac{1}{\rho_i^2} + \frac{1}{\rho_w^2} \right) M(R, R_c, h) \mathbf{n}. \tag{34}$$

Here we have the dimensionless factor

$$M(R, R_c, h) = \exp(-A_+^2)(1+C) - \exp(-A_-^2)(1-C), \tag{35}$$

where we have also defined

$$C = \frac{2RR_c}{h^2}. \tag{36}$$

Thus, the reversible contribution to the equation of motion near a spherical object has the form

$$\begin{aligned}
m_i \frac{d\mathbf{v}_i}{dt} \Big|_{\text{press}} & = \sum_{j, \text{fluid}}^{N_f} m_i m_j \left(\frac{p_i}{\rho_i^2} + \frac{p_j}{\rho_j^2} \right) \mathbf{r}_{ij} F_{ij} \\
& + \frac{\rho_w m_i h p_i}{2R^2 \pi^{1/2}} \left(\frac{1}{\rho_i^2} + \frac{1}{\rho_w^2} \right) M(R, R_c, h) \mathbf{n}.
\end{aligned} \tag{37}$$

In colloidal simulations, this additional force prevents fluid particles from penetrating the suspended spheres. By symmetry, the colloidal particle experiences a force equal and opposite in

direction to the boundary force experienced by the fluid particle. The full equations of motion for a suspended sphere are summarized in Section 8.

The pressure field at the surface of a moving sphere exerts a net force on the particle, and we use this drag force to validate the integrated pressure expression. In particular, we compute the drag on a solid sphere in uniform flow using the present numerical approach and compare it to the expected result from Stokes' law. This is done by initializing a lattice of SDPD fluid particles and placing a colloidal particle inside the box. Pressures are assigned to the fluid particles surrounding the colloid according to the pressure field solution for Stokes' flow around a sphere, and the force on the colloidal particle is calculated by summing the pair interaction given by Eq.(34) over all fluid-colloid pairs. As a reference fluid for these tests, we use parameters for a Lennard-Jones fluid at temperature $T = 1.0$ and density $\rho = 0.8$, with non-dimensional units as

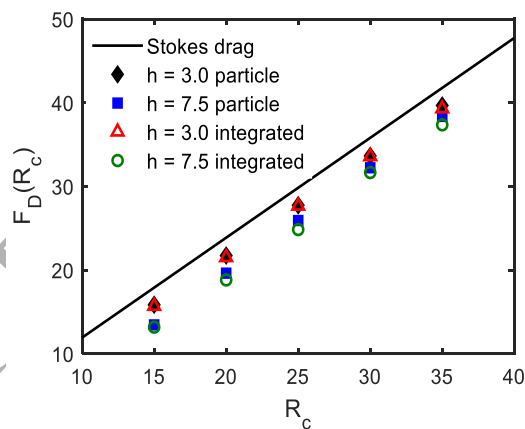


Fig. 4. Drag force acting on spherical particle in uniform flow due to pressure distribution at particle surface. The analytical solution (black line) is compared to the drag on the particle calculated numerically using traditional boundary particle techniques (diamond/square markers), and using the integrated boundary approach (hollow triangle and circle markers). For the numerical ghost particle and integrated boundary results, we show data for two different fluid resolutions, a fine case where fluid particles have a smoothing length of $h = 3.0$, and a more coarse one where $h = 7.5$.

described in Ref. [51]. At this thermodynamic state, the fluid viscosity is $\eta = 1.9$ [52]. We choose $\kappa = 4$ for the influence domain of the fluid particles.

We consider two different resolutions for the fluid, one where the fluid particles have mass and smoothing length $m = 12.5$ and $h = 3.0$, respectively, and one with $m = 200.0$ and $h = 7.5$. For the first case, the 64000 particles are initialized on a $40 \times 40 \times 40$ lattice inside a simulation box with dimensions $100 \times 100 \times 100$. For the coarser test, 4096 particles are placed on a $16 \times 16 \times 16$ inside a volume with side lengths $100 \times 100 \times 100$. After the lattice is prepared, a solid sphere with some radius is placed at the center of the simulation box, and fluid particles located inside the colloid are deleted. Note that particles are held at their initial positions after initialization and only the instantaneous force based on the pressure field is computed; hence, as the colloid's radius is adjusted, the distance of the nearest shell of particles around the boundary changes, affecting the error in the integral and sum approximations.

The influence of the particle distribution on the numerical accuracy is the so-called “particle inconsistency” issue in SPH [53]. For an accurate solution, each particle must have ~ 56 neighbors within its support domain [4]. Moreover, for an incompressible fluid, the distribution of particles in space should be relatively uniform, and both of these aspects introduce error in the solution. To reduce this effect, when creating the lattice we place particles randomly within $0.4dx$ of the ideal cubic lattice site, where dx is the lattice spacing. We initialize 10 independent random initial fluid particle distributions, and data points are obtained from an average over this ensemble of fluid particle configurations. Following this initialization of particle positions, pressures are assigned to the fluid particles using the Stokes flow solution for uniform flow past a sphere, i.e., we calculate the distance r of every fluid particle from the colloid center and give it a pressure according to [54]

R_c	$\langle N_w \rangle$	$\langle \Delta N_{pair} \rangle$	$\langle F_{int} \rangle$	$\langle F_{par} \rangle$	$\langle F_{actual} \rangle$	$\langle F_{int} \rangle$ % error	$\langle F_{par} \rangle$ % error
15	908	495293	15.693	15.860	17.907	12.364	11.434
20	2151	907161	21.520	21.746	23.876	9.870	8.923
25	4193	1434890	27.671	27.754	29.845	7.286	7.536
30	7244	2081535	33.581	33.660	35.814	6.237	6.014
35	11510	2853274	39.302	39.676	41.783	5.938	5.043

Table 1. Results from Stokes' flow simulations for the drag force on a spherical colloid. The brackets indicate averaging over an ensemble of 10 fluid particle initial configurations. We provide the colloid radius R_c , the corresponding average number of fluid particles deleted when creating the colloid N_c (i.e., those that fall inside it), the reduction in pair interactions when going from the traditional boundary approach to integrated boundaries $\langle \Delta N_{pair} \rangle$, the average drag force calculated using the integrated boundary approach F_{int} , the force from the traditional ghost particle method F_{par} , the actual force F_{actual} from the analytical result, and finally the percent error in F_{int} and F_{par} relative to the analytical solution. All numerical results shown are for the $h = 3.0$ case.

$$p' = P_0 - \frac{3\eta U_\infty}{2R_c} \left(\frac{R_c}{r} \right)^2 \cos \theta. \quad (38)$$

U_∞ is the velocity far from the sphere, assumed in the z -direction; for the present calculations we assume $U_\infty = 0.1$. P_0 is the static fluid pressure far from the sphere, which has no effect on the drag encountered by the sphere and we set it to zero for convenience. Once a pressure has been assigned to every fluid particle, we calculate the instantaneous force acting on the colloid by summing Eq.(34) over neighboring fluid particles. The computed drag from this calculation is compared to the analytical result for Stokes' drag around a sphere due to the dynamic distribution of pressure on the sphere's surface [54],

$$\mathbf{F}_D = 2\pi\eta R_c U_\infty \mathbf{e}_z. \quad (39)$$

In addition to using the integrated boundary approach, we also perform a control test using the same SDPD calculations but without deleting the fluid particles inside the colloid,

instead converting those fluid particles to boundary “ghost” particles and using traditional boundary particle techniques. For straightforward comparison to our integrated boundary results, we use a truncated Gaussian kernel for the SDPD particle-particle interactions. Table 1 summarizes the number of ghost particles $\langle N_c \rangle$ comprising the colloid for each case, as well as the reduction in pair interactions between the integrated and traditional particle calculations. In other words, we find the number of pair interactions needed to calculate the drag on the spherical particle using traditional boundary strategies, and then we determine the number of pair interactions necessary to compute the drag using integrated boundaries. The difference between these two quantities $\langle \Delta N_{pair} \rangle$ is the reduction in the number of pair interactions when using integrated boundaries versus traditional techniques. We find that our numerical calculation of the pair interaction reduction exactly follows the $\sim R_c^2$ scaling discussed in Section 1. For the test involving larger colloids and $h = 3.0$ resolution, using integrated boundaries requires 2 million fewer pair force calculations than the standard ghost particle approach.

Fig. 4 compares the drag force on the spherical particle computed using integrated boundaries to the result obtained using traditional boundary particle methods, and to the analytical result given by Eq.(39). Actual values for the drag computed using boundary ghost particles $\langle F_{par} \rangle$, integrated boundaries $\langle F_{int} \rangle$, and the known analytical solution $\langle F_{actual} \rangle$ are also provided in Table 1. The error in the integrated boundary calculation versus the analytical solution is also listed in the table. For a fixed fluid resolution, we find that the error in the integrated boundary solution decreases with increasing colloid radius, since the fluid particles with fixed resolution are able to more accurately resolve the flow field around the particle as the radius of curvature of the colloid increases relative to the particles. As expected, increasing the

resolution of the fluid from $h = 7.5$ to $h = 3.0$ dramatically decreases the error. The integrated boundary results for the $h = 3.0$ case are typically under 10%, except for the largest error at 12.4% for the smallest colloid tested ($R_c = 15$). The lowest error is 5.9% for the largest ($R_c = 35$). The errors when using integrated boundaries are comparable to the ones with traditional boundary techniques, where the largest and smallest errors (again corresponding to the smallest and largest particles) are 11.4% and 5.0%, respectively. While the standard ghost particle approach is slightly more accurate due to providing a uniform particle description throughout the system, this improvement in accuracy is extremely modest while requiring considerably more calculations.

5. Second Derivative Approximation for Viscous Term

The Laplacian of a scalar or vector field appears in the transport equations for momentum and solute diffusion, and hence integrated boundaries must approximate this quantity near surfaces. In other words, we now consider the integrated boundary contribution that corresponds to the second term in Eq.(5), the viscous interaction between a fluid particle and nearby wall or colloid. In the integral approximation, the Laplacian is typically written as [3]

$$\langle \nabla \cdot (k \nabla f) \rangle = -2k \int_{\Omega} [f(\mathbf{r}) - f(\mathbf{r}')] F(|\mathbf{r} - \mathbf{r}'|) d\mathbf{r}'. \quad (40)$$

As in the previous section, we separate this integral into fluid and wall contributions, and focus on the latter,

$$-2k [f(\mathbf{r}) - f_w] \int_{\Omega_w} F(|\mathbf{r} - \mathbf{r}'|) d\mathbf{r}'. \quad (41)$$

Dirichlet boundary conditions are again assumed, and we now compute analytical expressions for planar and spherical boundaries that are straightforwardly incorporated into the equations of motion for the fluid particles.

5.1. Fluid Particle near Planar Boundary

It is necessary to modify the function difference in Eq.(41) by extrapolating the function into the boundary similar to the particle extrapolation in Eq.(8),

$$-2k [f(\mathbf{r}) - f_w] \int_{\Omega_w} \left(1 + \frac{\Delta z'}{\Delta z}\right) F(|\mathbf{r} - \mathbf{r}'|) d\mathbf{r}'. \quad (42)$$

Here, Δz is the distance of the point \mathbf{r} from the boundary (where \mathbf{r} is located inside the fluid region), and $\Delta z'$ is the distance of the point \mathbf{r}' from the boundary (where $\mathbf{r}' \in \Omega_w$). The correction factor $\beta = 1 + \Delta z' / \Delta z$ ensures that the value of the function f_w is strictly enforced at the desired surface.

As in Section 3, we use spherical coordinates with the origin set at the point in the fluid \mathbf{r} where the function is approximated to obtain an exact result for a truncated Gaussian kernel. In spherical coordinates, the distance between a point \mathbf{r}' inside the solid and a planar boundary is given by

$$\Delta z' = r \cos \theta - \Delta z. \quad (43)$$

Substituting Eq.(43) into Eq.(42) and writing the integral explicitly gives

$$-2k [f(\mathbf{r}) - f_w] \int_{\Delta z}^{kh} dr \int_0^{2\pi} d\phi \int_0^{\theta_0} d\theta \left(\frac{r \cos \theta}{\Delta z}\right) F(r) r^2 \sin \theta. \quad (44)$$

with $\theta_0 = \cos^{-1}(\Delta z / r)$. Introducing the expression for $F(r)$ given by Eq.(27) and integrating gives the final result for the wall term,

$$-\frac{2k}{\pi^{1/2}h\Delta z} [f(\mathbf{r}) - f_w] K\left(\frac{\Delta z}{h}\right). \quad (45)$$

Here, we have defined the dimensionless quantity

$$K\left(\frac{\Delta z}{h}\right) = \exp\left(-\frac{\Delta z^2}{h^2}\right) + \exp(-\kappa^2) \left[\frac{\Delta z^2}{h^2} - (1 + \kappa^2) \right]. \quad (46)$$

Note that if we had integrated over all space (i.e. the approximation $\kappa \rightarrow \infty$), this equation simplifies to $K(\Delta z / h) = \exp(-\Delta z^2 / h^2)$. Due to the exponentially decaying kernel, the boundary contribution beyond the radius κh is generally small, and therefore this approximation is often useful.

As an example, the Laplacian boundary term in Eq.(45) is applied to each component of the velocity vector to enforce no-slip in simulations involving incompressible flows past a planar boundary, in which case the equations of motion [Eq.(5)] become

$$m_i \frac{d\mathbf{v}_i}{dt} = - \sum_{j, \text{fluid}}^{N_f} m_i m_j \left(\frac{p_i}{\rho_i^2} + \frac{p_j}{\rho_j^2} \right) \frac{\partial W_{ij}}{\partial r_{ij}} \mathbf{e}_{ij} + 2\eta \sum_{j, \text{fluid}}^{N_f} \frac{m_i m_j}{\rho_i \rho_j} \left(\frac{1}{|\mathbf{r}_{ij}|} \frac{\partial W_{ij}}{\partial r_{ij}} \right) \mathbf{v}_{ij} - \frac{2m_i \eta (\mathbf{v}_i - \mathbf{v}_w)}{\rho_i \pi^{1/2} h \Delta z_i} K\left(\frac{\Delta z_i}{h}\right). \quad (47)$$

Note that the boundary term diverges in the limit $\Delta z_i \rightarrow 0$, a consequence of the linear extrapolation of the function into the boundary described by Eq.(8). Large forces arising from lack of numerical precision are typically avoided by capping the factor $\beta = 1 + \Delta z' / \Delta z$ [6]. Some work suggests that integrated boundaries work well for compressible fluids and moderate

Reynold's numbers, but may be unstable for low Reynold's number incompressible flows [6], though we do not encounter any such issues in our tests below.

5.2. Particle near Spherical Boundary

We now derive an expression for the Laplacian near a spherical object, which can be used to apply a no-slip condition at the surface of a colloidal particle. In this case, the integral in Eq.(41) is

$$-2k [f(\mathbf{r}) - f_w] \int_{R-R_c}^{R+R_c} dr \int_0^{2\pi} d\phi \int_0^{\theta_0} d\theta \left(1 + \frac{\Delta z'}{\Delta z}\right) r^2 \sin \theta F(r). \quad (48)$$

The integration limit θ_0 is specified through the relationship $R_c^2 = R^2 + r^2 - 2rR \cos \theta_0$, where R_c is the radius of the spherical object, R is the separation between the center-of-mass of the sphere and point in the fluid \mathbf{r} . Substituting into Eq.(48) and integrating over θ and ϕ ,

$$-\frac{2\pi k}{R-R_c} [f(\mathbf{r}) - f_w] \int_{R-R_c}^{R+R_c} dr r^3 F(r) \left[1 - \left(\frac{R^2 + r^2 - R_c^2}{2rR}\right)^2\right]. \quad (49)$$

It is straightforward to obtain an exact analytical solution by replacing the upper limit in the integral in Eq.(49) with κh . For simplicity, we integrate over the entire colloidal particle after substituting Eq.(27) into Eq.(49), arriving at the result,

$$-\frac{hk}{\pi^{1/2} R^2 (R-R_c)} [f(\mathbf{r}) - f_w] M(R, R_c, h). \quad (50)$$

For simulations of fluid flow near a sphere, no-slip is applied by modifying Eq.(5) and including the boundary term to give

$$\begin{aligned}
m_i \frac{d\mathbf{v}_i}{dt} = & - \sum_{j, \text{fluid}}^{N_f} m_i m_j \left(\frac{p_i}{\rho_i^2} + \frac{p_j}{\rho_j^2} \right) \frac{\partial W_{ij}}{\partial r_{ij}} \mathbf{e}_{ij} \\
& + 2\eta \sum_{j, \text{fluid}}^{N_f} \frac{m_i m_j}{\rho_i \rho_j} \left(\frac{1}{|\mathbf{r}_{ij}|} \frac{\partial W_{ij}}{\partial r_{ij}} \right) \mathbf{v}_{ij} - \frac{\eta m_i h (\Delta \mathbf{v}_i - R_c \boldsymbol{\omega} \times \mathbf{n})}{\rho_i \pi^{1/2} R^2 (R - R_c)} M(R, R_c, h).
\end{aligned} \tag{51}$$

In this equation, $\boldsymbol{\omega}$ is the angular velocity of the sphere, \mathbf{n} is a normal vector pointing from the colloid center towards the fluid particle, and we have defined $\Delta \mathbf{v}_i = \mathbf{v}_i - \mathbf{V}_c$, where \mathbf{V}_c is the linear velocity of the sphere center of mass. Following Newton's third law, the colloid receives a contribution to its equation of motion due to the i th particle given by

$$M_c \frac{d\mathbf{V}_c}{dt} = \frac{\eta m_i h (\Delta \mathbf{v}_i - R_c \boldsymbol{\omega} \times \mathbf{n})}{\pi^{1/2} \rho_i R^2 (R - R_c)} M(R, R_c, h). \tag{52}$$

Here, M_c is the total mass of the colloidal particle. The full equations of motion for the colloid are given in Section 8.

As in the previous section, we test Eq.(52) by calculating the drag on a solid sphere in uniform flow using integrated boundaries and contrast it to the result from Stokes' law and the standard boundary particle SDPD approach. Once more, we place a colloid inside the simulation box after initializing a lattice of SDPD fluid particles. Following this step, a velocity is assigned to each fluid particle using the flow field solution for Stokes' flow around a sphere. The drag on the colloidal particle is determined from the sum of interactions between the surrounding fluid particles and the colloid, given by Eq.(52). We again use parameters for a Lennard-Jones fluid at the same thermodynamic state and consider two cases: 1) a finely-resolved fluid having particles with mass $m = 12.5$ and smoothing length $h = 3.0$, and 2) a more coarse test where the fluid is discretized into particles with mass $m = 200.0$ and $h = 7.5$. The first case uses particles initialized on a $40 \times 40 \times 40$ lattice inside a simulation box with side lengths of $100 \times 100 \times 100$, while the

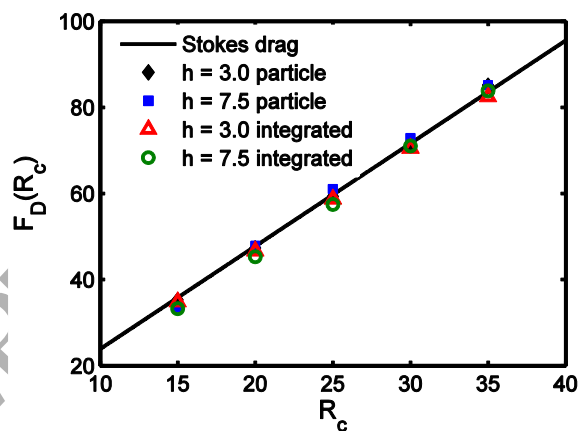


Fig. 5. Total force acting on spherical particle in uniform flow due to viscous forces versus particle radius. The black curve is the analytical result in the Stokes flow limit. Once again, this solution is compared to the numerically-computed drag on the particle, determined using traditional boundary particle techniques (diamond and square markers) and the same calculation using the integrated boundary approach (hollow triangle and circle markers). For the numerical results, we show data for two different cases, one where fluid particles have a smoothing length of $h = 3.0$, and another with $h = 7.5$.

R_c	$\langle F_{int} \rangle$	$\langle F_{par} \rangle$	$\langle F_{actual} \rangle$	$\langle F_{int} \rangle$ % error	$\langle F_{par} \rangle$ % error
15	34.871	35.300	35.814	2.634	1.435
20	46.645	47.329	47.752	2.318	0.886
25	58.710	59.276	59.690	1.642	0.694
30	70.523	71.178	71.628	1.543	0.628
35	82.465	85.156	83.566	1.318	1.902

Table 2. Summary of results from Stokes' flow calculations for the net force acting on spherical colloid due to viscous interactions. Brackets denote averaging over an ensemble of fluid particle initial configurations. The table lists the colloid radius R_c , the average force calculated using the integrated boundary approach F_{int} , the force from the traditional ghost particle method F_{par} , the actual force F_{actual} from the analytical result, and finally the percent error in F_{int} and F_{par} relative to the analytical solution. Results shown are for the $h = 3.0$ case.

second uses particles created on a $16 \times 16 \times 16$ inside a volume with dimensions $100 \times 100 \times 100$, and we consider an ensemble of random particle configurations by giving particles random displacements from their initial positions with magnitude $0.4dx$. Particles that overlap with the colloid are removed from the simulation after a sphere with radius R_c is introduced at the center of the box.

With particle positions relative to the colloid known, velocities are assigned to the fluid particles using the Stokes' flow solution for flow past a spherical object, i.e., we assign a velocity to each particle based on its position according to [54]

$$\begin{aligned}
 v_r(r, \theta) &= U_\infty \cos \theta \left[1 - \frac{3}{2} \left(\frac{R_c}{r} \right) + \frac{1}{2} \left(\frac{R_c}{r} \right)^3 \right], \\
 v_\theta(r, \theta) &= -U_\infty \sin \theta \left[1 - \frac{3}{4} \left(\frac{R_c}{r} \right) - \frac{1}{4} \left(\frac{R_c}{r} \right)^3 \right].
 \end{aligned} \tag{53}$$

After a velocity is given to every fluid particle, we find the force acting on the colloid by summing Eq.(52) over nearby fluid particles and compare it to the analytical creeping flow result for the drag, which, neglecting the pressure contribution, is given by [54]

$$\mathbf{F}_D = 4\pi\eta R_c U_\infty \mathbf{e}_z. \quad (54)$$

For completeness, we again perform the equivalent test using the same SDPD calculations but using traditional boundary particle techniques. In this case, we only sum the viscous interactions between ghost-fluid particle pairs to determine the total force acting on the colloid, which is now composed of a collection of SDPD particles. The results for the integrated boundary case, the one using ghost boundary particles, and the analytical result are summarized in Table 2 and Fig. 5.

We report values for three different error contributions: 1) the overall numerical error, calculated by comparing the mean drag force computed numerically to the analytical result given by Eq.(54) (see Table 2), 2) the error due to the particle distribution, which is related to the deviation of the drag force obtained from the 10 independent initial configurations compared to the mean, and 3) the error from not using a uniform particle description, determined by computing the integrated boundary drag force to the force obtained using traditional boundary techniques. Table 2 summarizes the data for the $h = 3.0$ tests and the associated overall errors for 1). The boundary ghost particle technique gives slightly more accurate results, with errors ranging between 0.6% and 1.9%, due to a consistent particle-based description. The error due to 3) of the integrated calculation relative to the equivalent particle case ranges between 0.9 and 3.2% for $h = 3.0$ and 0.7 and 5.9% for $h = 7.5$. However, the gain in accuracy due to using a uniform particle model throughout is generally modest and comes at significant computational cost. Finally, we investigate how the distribution of the particles affects the error 2) by

comparing the deviations in the drag force computed from the different random initial configurations relative to the mean. For the $h = 3.0$ tests, the difference from the mean drag force due to the random arrangement of particles is small and always less than 1.1%. The smallest is 0.4% for the $R_c = 25$ case, and the largest is 1.1% for $R_c = 15$. By comparison, the same error using the traditional boundary method ranges between 0.1 and 0.4%. As expected, the errors for the less finely-resolved $h = 7.5$ case are larger, with ranges for the deviation in the drag force of 0.8 and 1.5% for the integrated boundary test and 0.3 and 1.4% for the particle one.

6. Integrated Torque Applied to Colloid Due to Surrounding Fluid

In Section 5 we derived the resultant force on the colloid, which acts on the center of mass of the sphere; with this location of the force action, we must compute the associated torque on the colloidal particle. The derivation in this section again proceeds from the particle perspective, where the colloid is composed of a lattice of subparticles that are later integrated out. Only the viscous interactions are relevant [second term on the right-hand-side of Eq.(5)], since the overall pressure force will exert a force along the vector joining the fluid particle and colloid center of mass and therefore not result in a net torque. Each viscous pair interaction between fluid particle and colloid subparticle exerts a torque about an axis passing through the colloid center of mass, which is given by the cross product of the displacement vector and force $\boldsymbol{\tau}_{ij} = \boldsymbol{\delta}_j \times \mathbf{f}_{ij}$. Here, $\boldsymbol{\delta}_j$ is the displacement vector pointing from the colloid center of mass to the j th colloid subparticle, $\boldsymbol{\delta}_j = \mathbf{r}_j - \mathbf{R}_c$, where \mathbf{R}_c is the position vector for the suspended sphere (Fig. 5). Using the viscous term in Eq.(5) and summing all torques due to each pair interaction

between particle i and ghost boundary colloid subparticle gives the total torque on the colloid due to the i th particle,

$$\boldsymbol{\tau}_i = -2\eta \sum_{j=1}^{N_w} \frac{F_{ij}}{v_i v_j} (\boldsymbol{\delta}_j \times \mathbf{v}_{ij}), \quad (55)$$

with $v_i = \rho_i / m_i$. Substituting the modified velocity difference

$\mathbf{v}_{ij} = \beta(\mathbf{v}_i - \mathbf{v}_s) = \beta(\Delta \mathbf{v}_i - R_c \boldsymbol{\omega} \times \mathbf{e}_z)$ and splitting into two sums,

$$\boldsymbol{\tau}_i = \frac{2\eta}{v_i v_w} \Delta \mathbf{v}_i \times \sum_{j=1}^{N_w} \beta F_{ij} \boldsymbol{\delta}_j + \frac{2\eta R_c}{v_i v_w} \sum_{j=1}^{N_w} \beta F_{ij} \boldsymbol{\delta}_j \times (\boldsymbol{\omega} \times \mathbf{e}_z). \quad (56)$$

The second term is rewritten using the vector triple product,

$$\boldsymbol{\delta}_j \times (\boldsymbol{\omega} \times \mathbf{e}_z) = \boldsymbol{\omega} (\boldsymbol{\delta}_j \cdot \mathbf{e}_z) - \mathbf{e}_z (\boldsymbol{\delta}_j \cdot \boldsymbol{\omega}), \quad (57)$$

giving

$$\boldsymbol{\tau}_i = \frac{2\eta}{v_i v_w} \Delta \mathbf{v}_i \times \sum_{j=1}^{N_w} \beta F_{ij} \boldsymbol{\delta}_j + \frac{2\eta R_c}{v_i v_w} \sum_{j=1}^{N_w} \beta F_{ij} \boldsymbol{\omega} (\boldsymbol{\delta}_j \cdot \mathbf{e}_z). \quad (58)$$

To simplify the expression, we used the fact that $\boldsymbol{\omega}$ is orthogonal to the displacement vector $\boldsymbol{\delta}_j$ (i.e. $\boldsymbol{\delta}_j \cdot \boldsymbol{\omega} = 0$), a consequence of the rigid body motion of the particle. Assuming a number density ν_w of subparticles that comprise the colloid, the sums in Eq.(58) can be replaced with the following integrals,

$$\boldsymbol{\tau}_i = \frac{2\eta}{\nu_i} \Delta \mathbf{v}_i \times \int_{\Omega_c} \beta F(|\mathbf{r}'|) \mathbf{r}' d\mathbf{r}' + \frac{2\eta R_c}{\nu_i} \boldsymbol{\omega} \int_{\Omega_c} \beta F(|\mathbf{r}'|) (\mathbf{r}' \cdot \mathbf{e}_z) d\mathbf{r}'. \quad (59)$$

We express these integrals explicitly using spherical coordinates by setting the coordinate origin at the center of the colloidal particle, with the unit vector in the z -direction \mathbf{e}_z pointing from the colloid center towards the i th fluid particle. In this case, the dot product in the second integral is $\mathbf{r}' \cdot \mathbf{e}_z = |\mathbf{r}'| \cos \theta$ and the scaling factor β for no-slip is

$$\beta = \left(1 + \frac{R_c - |\boldsymbol{\delta}_j| \cos \theta}{R - R_c} \right). \quad (60)$$

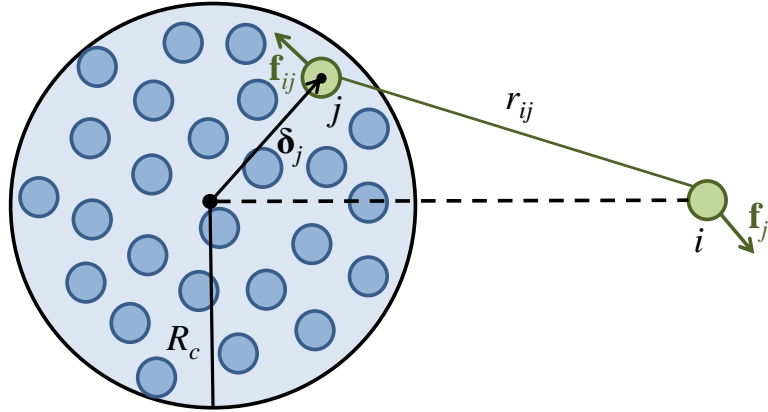


Fig. 5. Illustration of variables when computing the torque on a colloidal sphere due to a single fluid particle i . In order to determine the total force acting on the colloid center of mass, we begin from the particle perspective, i.e. the colloid is decomposed into a collection of particles. We write the sum of forces acting on the colloid center of mass, and then replace the summation with an integral.

First we address the first integral on the right-hand-side of Eq.(59). Note that the vector \mathbf{r}' is given by

$$\mathbf{r}' = r\mathbf{e}_r = r \sin \theta \cos \phi \mathbf{e}_x + r \sin \theta \sin \phi \mathbf{e}_y + r \cos \theta \mathbf{e}_z. \quad (61)$$

With our choice for the coordinate system centered inside the colloid, it is necessary to evaluate a separate integral for each of the three components of \mathbf{r}' ,

$$\begin{aligned} & \frac{2\eta}{v_i} \Delta \mathbf{v}_i \times \mathbf{e}_x \int_0^{R_c} dr \int_0^{2\pi} d\phi \int_0^\pi d\theta \left(1 + \frac{R_c - r \cos \theta}{R - R_c} \right) F(r, \theta) r^3 \sin^2 \theta \cos \phi \\ & + \frac{2\eta}{v_i} \Delta \mathbf{v}_i \times \mathbf{e}_y \int_0^{R_c} dr \int_0^{2\pi} d\phi \int_0^\pi d\theta \left(1 + \frac{R_c - r \cos \theta}{R - R_c} \right) F(r, \theta) r^3 \sin^2 \theta \sin \phi \\ & + \frac{2\eta}{v_i} \Delta \mathbf{v}_i \times \mathbf{e}_z \int_0^{R_c} dr \int_0^{2\pi} d\phi \int_0^\pi d\theta \left(1 + \frac{R_c - r \cos \theta}{R - R_c} \right) F(r, \theta) r^3 \sin \theta \cos \theta. \end{aligned} \quad (62)$$

Here, we have also substituted Eq.(60). We recognize that, due to our choice of coordinate origin, the function F now depends on both r and θ ,

$$F(r, \theta) = \frac{2}{\pi^{3/2} h^5} \exp \left[-\frac{r^2 + R^2 - 2rR \cos \theta}{h^2} \right]. \quad (63)$$

Integrating Eq.(62) with respect to ϕ , two of the integrals vanish due to the antisymmetry of the integrand, and only the z -component (i.e. the vector joining the centers of the colloid and the fluid particle) remains,

$$\frac{4\pi\eta}{v_i} \Delta \mathbf{v}_i \times \mathbf{e}_z \int_0^{R_c} dr \int_0^\pi d\theta \left(1 + \frac{R_c - r \cos \theta}{R - R_c} \right) F(r, \theta) r^3 \sin \theta \cos \theta. \quad (64)$$

Note that the unit vector \mathbf{e}_z appears in this expression due to our choice of coordinates for the integration such that the unit vector pointing from the colloid towards the fluid particle is in the z -direction. More generally, this vector is a normal vector pointing from the center of the colloid towards the fluid particle, regardless of the location of the fluid particle with respect to it. We

therefore introduce a surface normal vector \mathbf{n} that henceforth replaces \mathbf{e}_z in the derivation. Substituting Eq.(63) into Eq.(64) and integrating, we obtain the final expression for the first integral in Eq.(59),

$$-\frac{\eta m_i (\Delta \mathbf{v}_i \times \mathbf{n})}{\rho_i \pi^{1/2} \hat{R}^3 (R - R_c)} B(\hat{R}, \hat{R}_c). \quad (65)$$

Above we have defined

$$B(\hat{R}, \hat{R}_c) = \exp(-A_+^2) \left(1 + \hat{R}^2 + C + \frac{1}{2} C^2 \right) - \exp(-A_-^2) \left(1 + \hat{R}^2 - C + \frac{1}{2} C^2 \right) + \sqrt{\pi} \hat{R}^3 G_+, \quad (66)$$

where

$$G_+(R) = \text{erf}(A_-) + \text{erf}(A_+). \quad (67)$$

We have also introduced the dimensionless quantities $\hat{R} = R/h$ and $\hat{R}_c = R_c/h$.

Next, we consider the second integral in Eq.(59), which is written explicitly in spherical coordinates as

$$\frac{2\eta R_c}{v_i} \omega \int_{\Omega_c} \beta F(|\mathbf{r}'|) |\mathbf{r}'| d\mathbf{r}' = \frac{2\eta R_c \rho_c}{v_i v_c (R - R_c)} \omega \int_0^{R_c} dr \int_0^{2\pi} d\phi \int_0^\pi d\theta (R - r \cos \theta) F(r, \theta) r^3 \sin \theta \cos \theta. \quad (68)$$

Substituting Eq.(63) into Eq.(68) and integrating,

$$-\frac{\eta R_c \omega}{v_i \pi^{1/2} \hat{R}^3 (R - R_c)} B(\hat{R}, \hat{R}_c). \quad (69)$$

Combining Eqs.(65) and (69), we arrive at the final result

$$\boldsymbol{\tau}_i = -\frac{\eta m_i (\Delta \mathbf{v}_i \times \mathbf{n} + R_c \boldsymbol{\omega})}{\rho_i h \pi^{1/2} \hat{R}^3 (\hat{R} - \hat{R}_c)} B(\hat{R}, \hat{R}_c). \quad (70)$$

As expected, the torque exerted on the colloid due to fluid particle i is a function of the colloid and fluid particle's linear velocity, the colloid's angular velocity, the separation of the fluid and colloid particles, the location of the fluid particle relative to the colloid, as well as constants including the colloidal particle radius, fluid density and viscosity, and fluid resolution (i.e. smoothing length). Eq.(70) is the torque acting on the colloid due to a single nearby fluid particle; the total torque on the colloid is the sum of the individual torques due to all of the surrounding fluid particles, $\tau_c = \sum_i \tau_i$ (see Section 8). Note that in SDPD, including the integrated boundary approach presented here, angular momentum is not conserved exactly. This is a standard approximation in SDPD since the spin associated with small particles is extremely

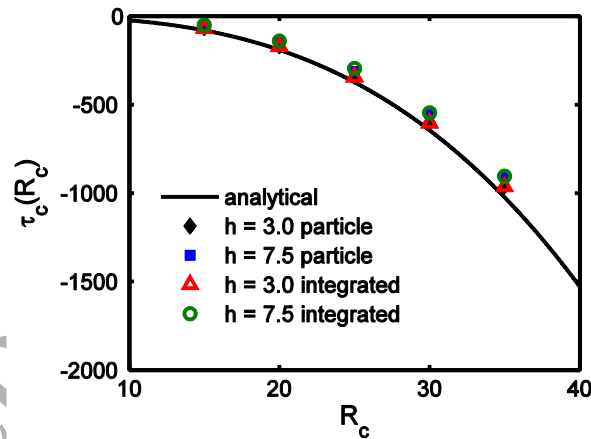


Fig. 7. The torque exerted on a stationary, non-rotating spherical particle in linear shear flow versus particle radius. The analytical result from Faxén's second law is shown as the black curve. This trend is exact in the zero Reynold's number limit, and compared to numerical calculations using SDPD. The diamond and square markers denote results using the traditional boundary particle method, and the hollow triangle and circle markers give the torque calculated using the integrated boundary approach. For the numerical calculations, we consider two different resolutions for the surrounding fluid, a case with $h = 3.0$ and one where $h = 7.5$

rapid in decaying to the local vorticity [15,47], though alternate formulations of SDPD that include a spin variable for each fluid particle have also been recently developed [55]. In the case of modeling flows having multiple colloidal spheres, ensuring angular momentum conservation may be crucial in some cases (e.g. dense suspensions or in presence of external force) [56], though for the current work where we consider a single particle this is sufficient. This study provides a foundation for future work where we will include momentum conservation in the rotational degrees of freedom through a spin variable [55] and apply this strategy to colloidal suspensions subjected to flow.

We test the integrated expression for the torque by placing a stationary, non-rotating colloidal particle inside a flow field, calculating the instantaneous torque on the colloid, and comparing to the analytical result. As in Section 5.2, a collection of SDPD fluid particles are initialized on a cubic lattice with spacing dx , and a colloidal particle is placed in the center of the simulation box. Ten separate particle configurations are initialized with independent random displacements from the ideal lattice positions, and fluid particles residing inside the colloid are deleted from the system. The remaining fluid particles are assigned a velocity based on the analytical solution in the zero Reynold's number limit for a particle in linear shear flow, where the spherical particle has no angular velocity [54]

$$\begin{aligned}
 v_r(r, \theta, \phi) &= \Gamma r \sin^2 \theta \sin \phi \cos \phi \left[1 - \frac{5}{2} \left(\frac{R_c}{r} \right)^3 + \frac{3}{2} \left(\frac{R_c}{r} \right)^5 \right], \\
 v_\theta(r, \theta, \phi) &= \Gamma r \sin \theta \cos \theta \sin \phi \cos \phi \left[1 - \left(\frac{R_c}{r} \right)^5 \right], \\
 v_\phi(r, \theta, \phi) &= -\frac{\Gamma r \sin \theta}{2} \left\{ 1 - \left(\frac{R_c}{r} \right)^3 - \cos 2\phi \left[1 - \left(\frac{R_c}{r} \right)^5 \right] \right\}.
 \end{aligned} \tag{71}$$

Γ is the shear rate. This solution corresponds to flow in the x -direction, and velocity gradient in the y -direction. The creeping flow result for the torque on the particle due to the above flow field is given by Faxén's second law, assuming no other colloids are present and zero angular velocity for the particle [54],

$$\boldsymbol{\tau}_c = -4\pi\eta R_c^3 \Gamma \mathbf{e}_z, \quad (72)$$

with the torque acting in the direction of the unperturbed flow vorticity.

In Fig. 7 we compare numerical results using the integrated boundary SDPD approach developed in this paper, averaged over the different random particle configurations, to the analytical result in Eq.(72). For a thorough comparison, we also include the same calculation using the traditional boundary ghost particle approach commonly employed in SPH and SDPD simulations. We find that errors are more significant when calculating the torque for both the integrated and boundary particle methods when compared to the linear force calculations in Section 5.2. As in Section 5.2, we consider three distinct errors in the torque: 1) the overall

R_c	$\langle \tau_{int} \rangle$	$\langle \tau_{par} \rangle$	$\langle \tau_{actual} \rangle$	$\langle \tau_{int} \rangle$ % error	$\langle \tau_{par} \rangle$ % error
15	-69.554	-69.600	-80.582	13.686	13.629
20	-170.971	-171.334	-191.009	10.490	10.301
25	-344.272	-343.595	-373.064	7.718	7.899
30	-604.070	-600.904	-644.655	6.296	6.787
35	-962.753	-964.297	-1023.688	5.952	5.802

Table 3. Summary of torques acting on non-rotating sphere in uniform shear flow. As before, brackets denote averages over an ensemble of fluid particle initial configurations. In this case, the table includes the average torque calculated using the integrated boundary approach τ_{int} , the torque from the traditional ghost particle method τ_{par} , the actual creeping flow torque τ_{actual} given by Faxén's 2nd law, and the percent error in the torque determined from the integrated and particle boundary techniques. The integrated and particle sum calculations are for the $h = 3.0$ case.

numerical error relative to the analytical solution [in this case Eq.(72)], 2) the error due to the particle distribution, determined from the average deviation of the individual initial configurations relative to the mean, and 3) the error due to not using a uniform particle description, which is calculated by comparing the results from the integrated boundary calculations to ones using traditional boundary methods. While the overall error 1) for the integrated boundary tests in Table 3 appear substantial, they are comparable in magnitude to ones obtained using the established ghost particle approach. For colloidal particles with radii of curvature greater than 25.0 and fluid particles with $h = 3.0$, the error 1) remains below 10% for both the integrated and boundary particle methods. For smaller colloids, a fluid composed of a higher number density of fluid particles is required to accurately resolve the flow around the highly curved particle in order to give the correct torque. When using particles with a larger smoothing length ($h = 7.5$), the inaccuracy in the torques is more significant, but still comparable to the error when using the ghost boundary particle method. The overall numerical errors for the $h = 3.0$ case are summarized in Table 3. The average error due to the particle distribution 2) for $h = 3.0$ ranges from 0.8 to 1.6%, depending on the colloid radius, whereas for the $h = 7.5$ case the range is from 1.4 to 2.5%. The error calculations for the equivalent test using the traditional boundary approach are between 0.3 and 0.8% for $h = 3.0$ and 1.0 and 3.1% for $h = 7.5$. The error due to not using a uniform particle description 3) is between 0.1 and 0.5% for $h = 3.0$ and 0.2 and 5.1% for $h = 7.5$.

7. Colloid Stochastic Force and Torque

Finally, we must consider the case in which the boundary can exchange momentum with the fluid due to random thermal stresses, i.e. we must determine the integrated boundary term for the final contribution to the SDPD equation of motion, Eq.(6). Including this stochastic contribution to the dynamics is essential when the boundary is a colloidal particle, in which case these fluctuations will result in its Brownian diffusion. We treat the boundary as a super-particle such that the fluctuations have the same structure as those between two fluid particles. For simplicity, we consider an incompressible Newtonian fluid and postulate noise in the velocity field of the form,

$$m_i d\tilde{\mathbf{v}}_i = \sum_{j, \text{fluid}}^N A_{ij} d\hat{\mathbf{W}}_{ij} \cdot \mathbf{e}_{ij} + \Upsilon_i d\hat{\mathbf{U}}_i \cdot \mathbf{n}. \quad (73)$$

Here, $d\mathbf{W}_{ij}$ and $d\mathbf{U}_i$ are dyadic tensors of Gaussian process increments. $d\hat{\mathbf{W}}_{ij}$ and $d\hat{\mathbf{U}}_i$ are the traceless, symmetric part of $d\mathbf{W}_{ij}$ and $d\mathbf{U}_i$, respectively. $d\hat{\mathbf{W}}_{ij}$ gives the stress between particles i and j , and $d\hat{\mathbf{U}}_i$ is the stress between the i th particle and the wall. Here, \mathbf{n} is the vector normal to the wall for a planar boundary. For a fluid particle near a spherical object, \mathbf{n} instead corresponds to a unit normal between the centers of particle i and the solid sphere. By symmetry, the colloidal particle experiences a force of $-\Upsilon_i d\hat{\mathbf{U}}_i \cdot \mathbf{n}$ due to its interaction with the i th particle. Ignoring the boundary terms, Eq.(73) reduces to the form of the noise for an incompressible SDPD fluid [15,21,48], Eq.(6). Above we assume that the stochastic fluid-boundary momentum exchange has the same structure as the random fluid-fluid interaction. This assumption is due to the fact that the integrated dissipative boundary terms have the same form as the viscous fluid-fluid force.

Following a derivation similar to the one in Refs. [15,16], it is possible to use the GENERIC formalism [12–14] to determine the correct form of the noise amplitudes A_{ij} and Υ_i in Eq.(73). The noise amplitude for the stochastic wall-fluid interaction for a planar boundary is

$$\Upsilon_i = \left[\frac{8k_B T m_i \eta}{\rho_i \pi^{1/2} h \Delta z_i} K \left(\frac{\Delta z_i}{h} \right) \right]^{1/2}. \quad (74)$$

If instead we consider a spherical object (e.g. colloid), the noise amplitude becomes

$$\Upsilon_i = \left[\frac{4\eta m_i h k_B T}{\rho_i \pi^{1/2} R^2 (R - R_c)} M(R, R_c, h) \right]^{1/2}. \quad (75)$$

Since there is a dissipative term that acts to reduce angular velocities, the fluctuation-dissipation theorem suggests that there is also a stochastic torque that introduces thermal noise in the angular momenta of the colloids. In other words, the stochastic interaction between fluid particle i and colloid subparticle pairs [Eq.(6)] results in a torque on the colloid, for which we postulate the form,

$$I_c d\tilde{\boldsymbol{\omega}} = T_i (d\hat{\mathbf{U}}_i \cdot \mathbf{n}) \times \mathbf{n}, \quad (76)$$

where I_c is the moment of inertia of the colloidal particle, which for a sphere is simply

$I_c = \frac{2}{5} M_c R_c^2$. The noise magnitude for fluctuation-dissipation is given by

$$T_i = \left[-\frac{4\eta m_i R_c k_B T}{\rho_i \pi^{1/2} \hat{R}^3 (R - R_c)} B(\hat{R}, \hat{R}_c) \right]^{1/2}. \quad (77)$$

8. Equilibrium Simulation of a Colloid Using Integrated Boundaries

In this section, we combine these results in a full simulation of a colloidal particle immersed in a fluid at thermal equilibrium undergoing Brownian motion, and hence validate the fluctuation-dissipation relationships given by Eqs.(75) and (77). We initialize a colloidal particle in a fluid modeled using a collection of SDPD volumes, then evolve the system in time and track the colloid's random walk. The interactions between all particles are pairwise and symmetric. Fluid particle pairs experience the normal SDPD interactions, summarized in Section 2. Fluid particles interact with the colloidal particle through conservative interactions due to the pressure field [(Eq.(34) in Section 4.2)], viscous forces due to friction [Eq.(51), Section VB], and random forces resulting from thermal fluctuations [Eq.(73), Section 7]. Since the colloid has rotational degrees of freedom, it also experiences stochastic torque according to Eq.(76), which is balanced by a dissipative term Eq.(70). Summarizing, the equation of motion for the colloidal sphere linear dynamics is

$$M_c d\mathbf{V}_c = - \sum_{j,fluid}^{N_f} \frac{\rho_w m_j h p_j}{2R^2 \pi^{1/2}} \left(\frac{1}{\rho_j^2} + \frac{1}{\rho_w^2} \right) M(R, R_c, h) \mathbf{n} dt + \sum_{j,fluid}^{N_f} \frac{\eta m_j h (\Delta \mathbf{v}_j - R_c \boldsymbol{\omega} \times \mathbf{n})}{\pi^{1/2} \rho_j R^2 (R - R_c)} M(R, R_c, h) dt + M_c d\tilde{\mathbf{V}}_c. \quad (78)$$

Here, $M_c d\tilde{\mathbf{V}}_c = - \sum_{j,fluid} Y_j d\hat{\mathbf{U}}_j \cdot \mathbf{n}$. The colloid's angular momentum is evolved using

$$I_c d\boldsymbol{\omega}_c = - \sum_{j,fluid}^{N_f} \frac{\eta m_j (\Delta \mathbf{v}_j \times \mathbf{n} + R_c \boldsymbol{\omega})}{\rho_j h \pi^{1/2} \hat{R}^3 (\hat{R} - \hat{R}_c)} B(\hat{R}, \hat{R}_c) dt + I_c d\tilde{\boldsymbol{\omega}}_c, \quad (79)$$

with $I_c d\tilde{\boldsymbol{\omega}}_c = \sum_{j,fluid} \mathbf{T}_j (d\hat{\mathbf{U}}_j \cdot \mathbf{n}) \times \mathbf{n}$. Densities of fluid particles near the colloid are updated using

Eq.(24). Note that Eq.(34) alone does not guarantee the kinematic boundary condition and particles may penetrate the boundary unless a prohibitively small time-step is used. Moreover,

the dissipative and random forces and torques diverge for zero separation between fluid particle and colloid $R = R_c$. For stability, fluid particles that penetrate the colloid ($R \leq R_c$) experience a constant repulsive pressure and dissipative forces equal to forces if the fluid particle was located a small distance outside the colloid $R = \Delta R$. For our numerical tests, we choose $\Delta R = 0.001$.

The simulation is constructed as follows: 3375 fluid particles are initialized on a $15 \times 15 \times 15$ lattice inside a $75 \times 75 \times 75$ volume. Each particle has a mass of $m = 100.0$, and the fluid density is $\rho = 0.8$, giving a smoothing length $h = 6.0$. For a consistent representation of fluid interactions, we use a truncated Gaussian kernel for the fluid-fluid particle interactions, with cut-off $\kappa = 4$. The parameters are chosen to represent a Lennard-Jones fluid at this mass density and temperature $T = 1.0$. At this thermodynamic state point, the shear viscosity is $\eta = 1.9$. After the fluid is initialized, we place a neutrally-buoyant (i.e. $\rho_w = 0.8$) colloidal particle in the center of the simulation box, and delete any fluid particles that overlap with it. Two independent tests are performed, one for a colloid with radius $R_c = 15$ and one with $R_c = 25$. The fluid and colloidal particle positions and velocities are integrated in time using the modified velocity Verlet algorithm in Ref. [57], and the colloid angular velocity is updated at the same time as the linear velocities. We use a time-step of $\Delta t = 0.001$, which ensures that fluid particle penetration of the colloid is infrequent, and equilibrate for 5.0×10^5 steps prior to starting the production run, which lasts for 1.5×10^6 steps. In Fig. 8 we show the probability distributions of a) linear and b) angular velocities adopted by the suspended sphere as it undergoes Brownian motion, and compare the results from the simulation to the Maxwell-Boltzmann distribution. The results from the simulation are in excellent agreement with this result, showing correct diffusive behavior. The error in the linear velocity distribution variance averaged over the x -, y -, and z -directions is 7.3%

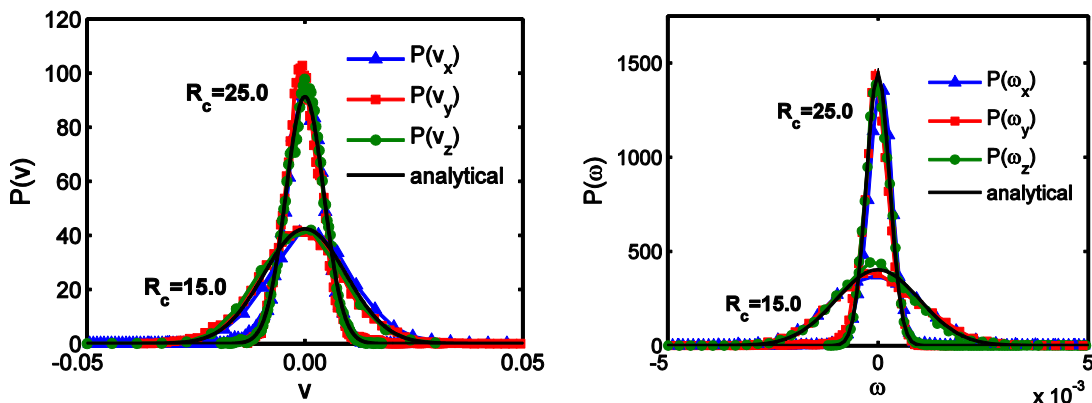


Fig. 8. (a) Probability distributions for colloid linear velocities from simulation of single Brownian sphere using the integrated boundary approach. (b) Distribution of suspended particle's angular velocities. The results are compared to the Maxwell-Boltzmann distribution.

for the $R_c = 15$ case and 5.7% for the $R_c = 25$ one. For the angular velocities, the error in the averaged variance is 11.8% and 17.6% for the $R_c = 15$ and 25 simulations, respectively.

9. Conclusions

SDPD provides a modeling framework for colloidal suspensions that does not make physical assumptions about the flow such as creeping flow ($Re \ll 1$) or diffusion-dominated regime ($Pe \ll 1$). This generality makes SDPD more numerically expensive than other strategies for modeling colloidal suspensions such as Brownian dynamics. Hence, techniques such as the integrated boundary framework presented in this paper, which dramatically reduces the number of pairwise force interactions calculated at each time-step, have the potential to significantly increase the practical utility of such methods. The boundary is achieved by decomposing a suspended particle in a fluid medium into a collection of SDPD boundary particles. These particles are subsequently integrated out, giving a single bulk contribution to the equation of

motion of a nearby fluid particle and the colloid center of mass, rather than determining pairwise forces between the fluid particle and each boundary one.

In Sections 5 and 6, we demonstrated that for low Reynold's number flows, this integrated approach gives results consistent with the analytical creeping flow solutions. Results are obtained for the cases of a spherical particle in uniform fluid flow, as well as a non-rotating spherical particle in shear flow, and the computed forces and torques are comparable to ones obtained from existing methods for enforcing no-slip in smoothed particle techniques. Section 7 introduces fluctuating forces and torques into the colloid's equation of motion, which are balanced by the dissipative forces and torques derived in the previous sections. Finally, in Section 8, we combine these elements and perform a full simulation of the Brownian motion of a single colloidal particle. The results show that the forms for the thermal noise in Section 7 give the correct relationship between the random and dissipative forces and torques, resulting in the expected Maxwell-Boltzmann distribution of linear and angular momenta for the suspended sphere.

The integrated boundary method leads to more efficient simulations of dispersed particles, but it is not without limitations. First, we found that forces and torques computed using integrated boundaries are slightly less accurate than ones obtained using traditional boundary particle techniques owing to the discrepancy in the fluid description in different parts of the simulation box when integrated objects are present. However, this increase in error is relatively small and a minor penalty for the computational speedup. In addition, Morris et al. suggest that integrated boundaries are well suited to compressible and moderate Reynold's number flows, but may be unstable in the creeping flow limit [6]. Another drawback of this approach is that analytical expressions for boundaries can only be obtained for simple geometries such as planar

surfaces and spheres, though objects with more complicated shapes can be pre-computed numerically and tabulated for use in simulations. It may be possible to obtain analytical results for ellipsoidal objects, which can approximate suspensions of rod-shaped particles. One final issue is that this approach does not perfectly conserve angular momentum. This will be remedied in future work by including a spin variable associated with the fluid particles, enabling more accurate simulations of suspension flows.

The integrated boundary strategy may be extended in a number of other ways. For example, our results assume no-slip, though analytical results for boundary conditions having a non-vanishing slip length may also be feasible. The presented approach is also easily extended to include more complicated physics. For example, integrated spherical objects can be tethered using a harmonic potential to model polymers, with each integrated sphere acting as a coarse-grained monomer. Furthermore, integrated expressions for spheres interacting through van der Waals and/or electrostatic interactions exist and may be straightforwardly included. For simulations of two or more Brownian spheres, a short-ranged repulsive lubrication force can be included, which acts along the line joining colloid particle centers and prevents their unphysical overlap, even if the actual SDPD fluid particles are excluded from the region that separates the two spheres [21]. DPD has already been used to probe the rheology of particle dispersions [36,37], and the integrated boundary approach in this paper presents an approach that allows for similar types of studies and is more rigorous while requiring fewer particles.

Finally, the integrated boundary SDPD framework described in this paper paves the way for simulations of suspensions that are more rigorous than ones using current DPD models while having reduced computational cost. DPD has been used to probe the rheology of suspensions [36,37]; using SDPD integrated boundary techniques, it is possible to develop a

parallelized code to investigate additional quantities in large systems, including the non-equilibrium structure and long-time dynamics of colloids. Moreover, these techniques are useful for modeling many important systems, including the advection and diffusion of nano- and microparticles inside the human body, particle-membrane interactions [58–60], drug vehicle transport through membranes [61], and the margination of nanoparticles in intravascular drug delivery [62,63]. SDPD has been previously used to investigate this type of phenomena [63], though when simulating biological systems the simulation size is often problematic, and our approach allows for larger systems due to the reduced particle number.

Acknowledgements

The authors gratefully acknowledge the support of the National Science Foundation (Award No. CBET-1256838) and a UCSB Chemical Engineering Dow Discovery Fellowship. Computational resources for this work were provided by the Center for Scientific Computing from the CNSI, MRL: an NSF MRSEC (DMR-1121053) and NSF CNS-0960316.

References

- [1] L. B. Lucy, *Astron. J.* **82**, 1013 (1977).
- [2] R. A. Gingold and J. J. Monaghan, *Mon. Not. R. Astron. Soc.* **181**, 375 (1977).
- [3] J. J. Monaghan, *Rep. Prog. Phys.* **68**, 1703 (2005).
- [4] G. R. Liu and M. B. Liu, *Smoothed Particle Hydrodynamics: A Meshfree Particle Method* (World Scientific Publishing Company, 2003).
- [5] J. J. Monaghan, *J. Comput. Phys.* **110**, 399 (1994).
- [6] J. P. Morris, P. J. Fox, and Y. Zhu, *J. Comput. Phys.* **136**, 214 (1997).
- [7] J. J. Monaghan and A. Kos, *J. Waterw. Port Coast. Ocean Eng.* **125**, 145 (1999).
- [8] A. Colagrossi and M. Landrini, *J. Comput. Phys.* **191**, 448 (2003).
- [9] M. Gómez-Gesteira and R. A. Dalrymple, **130**, 63 (2004).

- [10] S. Marrone, A. Colagrossi, M. Antuono, C. Lugni, and M. P. Tulin, *J. Fluids Struct.* **27**, 1199 (2011).
- [11] S. Marrone, B. Bouscasse, A. Colagrossi, and M. Antuono, *Comput. Fluids* **69**, 54 (2012).
- [12] M. Grmela and H. C. Öttinger, *Phys. Rev. E* **56**, 6620 (1997).
- [13] H. C. Öttinger and M. Grmela, *Phys. Rev. E* **56**, 6633 (1997).
- [14] H. C. Öttinger, *Beyond Equilibrium Thermodynamics* (Wiley-Interscience, Hoboken, N.J., 2005).
- [15] P. Español and M. Revenga, *Phys. Rev. E Stat. Nonlin. Soft Matter Phys.* **67**, 026705 (2003).
- [16] N. D. Petsev, L. G. Leal, and M. S. Shell, *J. Chem. Phys.* **144**, 084115 (2016).
- [17] A. Vázquez-Quesada, M. Ellero, and P. Español, *J. Chem. Phys.* **130**, 034901 (2009).
- [18] S. Litvinov, M. Ellero, X. Hu, and N. A. Adams, *Phys. Rev. E* **77**, 066703 (2008).
- [19] S. Litvinov, X. Y. Hu, and N. A. Adams, *J. Phys. Condens. Matter* **23**, 184118 (2011).
- [20] N. Moreno, P. Vignal, J. Li, and V. M. Calo, *Procedia Comput. Sci.* **18**, 2565 (2013).
- [21] X. Bian, S. Litvinov, R. Qian, M. Ellero, and N. A. Adams, *Phys. Fluids* **24**, 012002 (2012).
- [22] M. Ferrand, D. R. Laurence, B. D. Rogers, D. Violeau, and C. Kassiotis, *Int. J. Numer. Methods Fluids* **71**, 446 (2013).
- [23] F. Macià, L. M. González, J. L. Cercos-Pita, and A. Souto-Iglesias, *Prog. Theor. Phys.* **128**, 439 (2012).
- [24] J. K. Chen, J. E. Beraun, and T. C. Carney, *Int. J. Numer. Methods Eng.* **46**, 231 (1999).
- [25] T. Belytschko, Y. Krongauz, D. Organ, M. Fleming, and P. Krysl, *Comput. Methods Appl. Mech. Eng.* **139**, 3 (1996).
- [26] G. R. Johnson and S. R. Beissel, *Int. J. Numer. Methods Eng.* **39**, 2725 (1996).
- [27] G. R. Johnson, R. A. Stryk, and S. R. Beissel, *Comput. Methods Appl. Mech. Eng.* **139**, 347 (1996).
- [28] F. Macià, M. Antuono, L. M. González, and A. Colagrossi, *Prog. Theor. Phys.* **125**, 1091 (2011).
- [29] H. Takeda, S. M. Miyama, and M. Sekiya, *Prog. Theor. Phys.* **92**, 939 (1994).
- [30] P. J. Hoogerbrugge and J. M. V. A. Koelman, *EPL Europhys. Lett.* **19**, 155 (1992).
- [31] P. Español and P. Warren, *EPL Europhys. Lett.* **30**, 191 (1995).
- [32] Z. Li, Y.-H. Tang, H. Lei, B. Caswell, and G. E. Karniadakis, *J. Comput. Phys.* **265**, 113 (2014).
- [33] H. Lei, D. A. Fedosov, and G. E. Karniadakis, *J. Comput. Phys.* **230**, 3765 (2011).
- [34] Z. Li, A. Yazdani, A. Tartakovsky, and G. E. Karniadakis, *J. Chem. Phys.* **143**, 014101 (2015).
- [35] T. Werder, J. H. Walther, and P. Koumoutsakos, *J. Comput. Phys.* **205**, 373 (2005).
- [36] E. S. Boek, P. V. Coveney, H. N. W. Lekkerkerker, and P. van der Schoot, *Phys. Rev. E* **55**, 3124 (1997).
- [37] E. S. Boek, P. V. Coveney, and H. N. W. Lekkerkerker, *J. Phys. Condens. Matter* **8**, 9509 (1996).
- [38] M. Whittle and E. Dickinson, *J. Colloid Interface Sci.* **242**, 106 (2001).
- [39] D. L. Ermak and J. A. McCammon, *J. Chem. Phys.* **69**, 1352 (1978).
- [40] J. F. Brady and G. Bossis, *Annu. Rev. Fluid Mech.* **20**, 111 (1988).
- [41] A. Sierou and J. F. Brady, *J. Fluid Mech.* **448**, 115 (2001).
- [42] D. R. Foss and J. F. Brady, *J. Fluid Mech.* **401**, 243 (1999).
- [43] T. N. Phung, J. F. Brady, and G. Bossis, *J. Fluid Mech.* **313**, 181 (1996).

- [44] A. J. C. Ladd, Phys. Rev. Lett. **70**, 1339 (1993).
- [45] A. J. C. Ladd and R. Verberg, J. Stat. Phys. **104**, 1191 (2001).
- [46] N. Sharma and N. A. Patankar, J. Comput. Phys. **201**, 466 (2004).
- [47] S. R. D. Groot and P. Mazur, *Non-Equilibrium Thermodynamics*, Dover edition (Dover Publications, New York, 2011).
- [48] X. Y. Hu and N. A. Adams, J. Comput. Phys. **213**, 844 (2006).
- [49] W. Dehnen and H. Aly, Mon. Not. R. Astron. Soc. **425**, 1068 (2012).
- [50] H. C. Hamaker, Physica **4**, 1058 (1937).
- [51] P. M. Kulkarni, C.-C. Fu, M. S. Shell, and L. Gary Leal, J. Chem. Phys. **138**, 234105 (2013).
- [52] K. Meier, A. Laesecke, and S. Kabelac, J. Chem. Phys. **121**, 3671 (2004).
- [53] M. B. Liu and G. R. Liu, Appl. Numer. Math. **56**, 19 (2006).
- [54] L. G. Leal, *Advanced Transport Phenomena: Fluid Mechanics and Convective Transport Processes*, 1st ed. (Cambridge University Press, 2010).
- [55] K. Müller, D. A. Fedosov, and G. Gompper, J. Comput. Phys. **281**, 301 (2015).
- [56] M. Yang, M. Theers, J. Hu, G. Gompper, R. G. Winkler, and M. Ripoll, Phys. Rev. E **92**, 013301 (2015).
- [57] R. D. Groot and P. B. Warren, J. Chem. Phys. **107**, 4423 (1997).
- [58] R. C. V. Lehn and A. Alexander-Katz, Soft Matter **7**, 11392 (2011).
- [59] R. C. V. Lehn, M. Ricci, P. H. J. Silva, P. Andreozzi, J. Reguera, K. Voitchovsky, F. Stellacci, and A. Alexander-Katz, Nat. Commun. **5**, 4482 (2014).
- [60] H. Ding and Y. Ma, Small **11**, 1055 (2015).
- [61] D. I. Kopelevich, J. Chem. Phys. **139**, 134906 (2013).
- [62] P. Decuzzi, S. Lee, B. Bhushan, and M. Ferrari, Ann. Biomed. Eng. **33**, 179 (2005).
- [63] K. Müller, D. A. Fedosov, and G. Gompper, Sci. Rep. **4**, (2014).